

## Understanding the Rheology of Polymer–Polymer Interfaces Covered with Janus Nanoparticles: Polymer Blends versus Particle Sandwiched Multilayers

Huawei Qiao, Botuo Zheng, Gang Zhong, Zhicong Li, Ruth Cardinaels, Paula Moldenaers, Khalid Lamnawar, Abderrahim Maazouz, Canpei Liu, and Huagui Zhang\*



Cite This: *Macromolecules* 2023, 56, 647–663



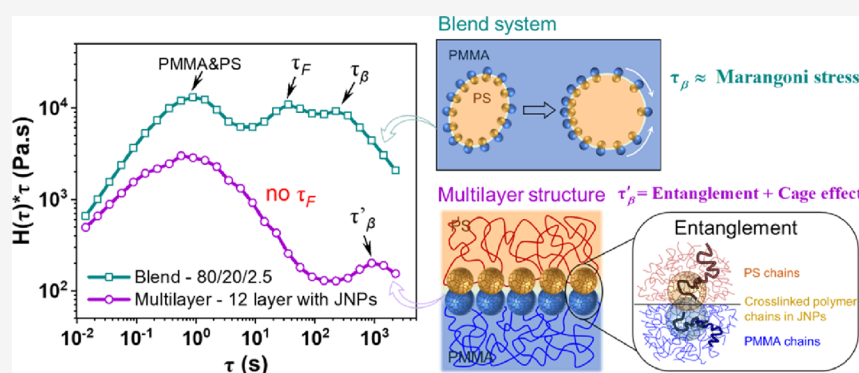
Read Online

ACCESS |

Metrics & More

Article Recommendations

Supporting Information



**ABSTRACT:** Interfacial rheology is crucial in dictating morphology and ultimate properties of particle-stabilized polymer blends, but is challenging to be determined. In this study, a fully polymeric dumbbell-shaped Janus nanoparticle (JNP) of polymethyl methacrylate (PMMA) and polystyrene (PS) spheres with equal sizes ( $\sim 80$  nm) was prepared and used as an efficient compatibilizer for PMMA/PS blends. The JNPs were preferentially localized at the PMMA/PS interface, thereby reducing the interfacial tension and refining the morphology in both droplet-matrix and co-continuous type blends, whereby a JNP concentration  $\sim 2.5$  wt % is sufficient to reach a saturation in droplet size reduction due to compatibilization. Based on the linear viscoelastic moduli and corresponding relaxation spectra ( $H(\tau)*\tau$ ) of JNP-compatibilized droplet-matrix blends, besides the droplet shape relaxation time ( $\tau_F$ ), a longer relaxation time ( $\tau_\beta$ ), typically related to interfacial viscoelasticity, was readily identified. The dependence of  $\tau_\beta$  on the JNP concentration ( $W_{\text{JNPs}}$ ) was significantly dominated by the droplet size reduction induced by the JNP compatibilization, with  $\tau_\beta$  decreasing with increasing  $W_{\text{JNPs}}$ . The viscoelastic properties extracted from  $\tau_\beta$  typically originate from a combination of gradients in interfacial tension due to the particle redistribution at the droplet interface (Marangoni stresses) and the deviatoric stresses of intrinsic rheological origin. The latter originate from the intrinsic viscoelasticity of the particle-laden interface, which is enhanced by particle jamming and particle–polymer interactions, such as entanglements between chains from the polymeric spheres and those penetrating from the bulk into the spheres. To address the challenge of isolating these contributions, a JNP-sandwiched PMMA/PS multilayer structure was designed to exclude the effect of Marangoni stresses and droplet curvature, thus having no  $\tau_F$  but a new relaxation ( $\tau'_\beta$ ), which characterizes the contribution of intrinsic interfacial viscoelasticity. The  $\tau'_\beta$  was observed to increase with JNP coverage ( $\Sigma$ ) following the Vogel–Fulcher–Tammann model that is typically used to describe the divergent behavior of the “cage” effect in classical colloidal glasses. Moreover, a multimode Maxwell model fitting allows to split the interfacial relaxation into the confined diffusion of JNPs within their cage and the entanglements between the JNPs and the bulk.

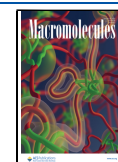
### 1. INTRODUCTION

Polymer blending is one of the most economical and attractive methods to obtain new materials with excellent properties. Nevertheless, the majority of polymers are immiscible, and their blends often have a phase-separated morphology, which can be discrete phase structures (droplets in a matrix) or co-continuous phase structures depending on the composition and processing conditions.<sup>1</sup> The strong thermodynamic driving forces often enable phase coalescence and/or coarsening

Received: September 25, 2022

Revised: December 19, 2022

Published: January 2, 2023



toward a macroscopic phase-separated state with a poor performance.<sup>2</sup> To refine and stabilize phase domains against coalescence and/or coarsening and hence retain a stable microscopic structure, compatibilizers are often used to reside at the interface between phases to enhance the phase compatibility.

One widely investigated compatibilizer type is block copolymers, composed of components of both bulk phases,<sup>3</sup> which are characterized by a great surface activity to preferentially accumulate at the interface and reduce the interfacial tension, while forming an interfacial layer with a certain thickness and elasticity. In the past decades, nanoparticles such as SiO<sub>2</sub>,<sup>4</sup> graphene,<sup>5</sup> clay,<sup>6</sup> and so forth have also been demonstrated to exhibit compatibilization to control the morphology of polymer blends. If being localized at the interface between both phases, the nanoparticles can exhibit a “Pickering effect”.<sup>7</sup> They can irreversibly anchor at the interface, thanks to their ultrahigh surface desorption energy, thus forming a robust interfacial film and act as a very effective stabilizer in inhibiting coalescence and coarsening. However, as most nanoparticles have no interfacial selectivity, they mainly reside in the bulk phase rather than at the interface. In recent years, Janus nanoparticles (JNPs), a class of nanoparticles having amphiphilic and/or anisotropic structures, have gradually attracted attention as compatibilizers in polymer blends.<sup>8–10</sup> Combining the amphiphilicity of a block copolymer and the Pickering effect of a nanoparticle, JNPs can not only be favorably driven to the interface between phases in a blend, but also exhibit a strong anchoring affinity once adsorbed at the interface, thereby avoiding being dragged into the bulk phases under the strong flow field during melt processing.

Apart from the reduction of the interfacial tension,<sup>11</sup> interest has shifted to the other roles of compatibilizers in inhibiting flow-induced coalescence between droplets including steric hindrance, Marangoni stresses at the droplet surface, and/or interfacial rheology.<sup>12–14</sup> Especially, block copolymers able to form an entangled thick copolymer layer or nanoparticles able to form a robust layer at the interface can act as a physical barrier to keep the droplets separated when they approach each other.<sup>15</sup> Marangoni effects (from interfacial tension gradients) are typically caused by concentration gradients of compatibilizers on the droplet surface.<sup>12,14</sup> In particular, as shown in Figure 1, when droplets approach each other, the matrix in the interdroplet region is forced to be squeezed out,

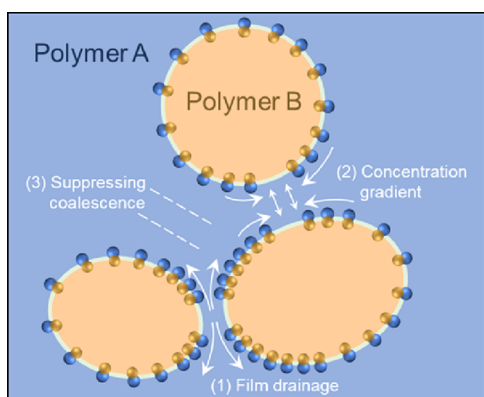


**Figure 1.** Schematic illustration of the Marangoni stress induced by JNPs located at the interface between both phases in a blend.

and the compatibilizers (e.g., JNPs) flow with the squeeze flow outward along the interface away from the contact region between the droplets, thereby generating a concentration gradient along the droplet interface. This concentration gradient generates a tangential stress directed to induce a redistribution of the compatibilizers at the interface to achieve a uniform stress state, thus slowing down or inhibiting the squeezing out of the matrix and consequently the droplet coalescence. Ha et al.<sup>16</sup> showed that very weak Marangoni stresses are sufficient to generate hydrodynamic forces that can inhibit drainage and thus coalescence.

In light of the intimate structure–rheology relations, small amplitude oscillatory shear (SAOS) measurements of polymer blends have proven to be sensitive to changes in morphology and interfacial properties, because of which they are frequently being used to evaluate compatibilization in blends.<sup>17–20</sup> For instance, as compared to the neat components, blends with a droplet-in-matrix morphology are often characterized by an enhanced elasticity at low frequencies with a distinct shoulder in the storage modulus ( $G'$ ) curve in linear viscoelasticity.<sup>19–21</sup> This  $G'$  shoulder is attributed to the shape relaxation of the dispersed phase, with a characteristic relaxation time denoted as  $\tau_F$ . Such shape relaxation is also measurable in blends with a co-continuous structure, whereby the enhanced elasticity at low frequencies is characterized by a power-law dependence of  $G'$  on frequency.<sup>22,23</sup> The addition of compatibilizers has been reported to alter the linear viscoelasticity of blends by shifting  $\tau_F$  toward a lower value (higher frequency) and introducing a more pronounced shape relaxation as a result of the reduction in droplet domain size and related increase of the interfacial area respectively.<sup>24,25</sup> More importantly, an additional interface-governed relaxation mechanism at a higher relaxation time ( $\tau_\beta$ ) than  $\tau_F$  was observed in the SAOS measurements of compatibilized blends.<sup>19,26</sup> Such interfacial viscoelasticity was mostly ascribed to the Marangoni stress of the interfacial compatibilizers<sup>19</sup> and argued to be linked to the interfacial shear modulus identified from the generalized version of the Palierne emulsion model. The latter was developed to describe the linear viscoelastic (LVE) behavior of droplet-matrix blends.<sup>27</sup> The model takes into account the droplet size, interfacial tension, and interfacial rheological properties to describe the complex modulus [ $G^*(\omega)$ ] of the blends with a constitutive equation expressed as:<sup>27</sup>

$$G^*(\omega) = G_m^*(\omega) \left[ \frac{1 + \frac{3}{2} \sum_i \frac{\phi_i E_i}{D_i}}{1 - \sum_i \frac{\phi_i E_i}{D_i}} \right] \quad (1)$$

$$\begin{aligned} E_i = & 2[G_d^*(\omega) - G_m^*(\omega)][19G_d^*(\omega) + 16G_m^*(\omega)] \\ & + \frac{48\beta_d^*(\omega)\Gamma}{R_i^2} + \frac{32\beta_s^*(\omega)[\Gamma + \beta_d^*(\omega)]}{R_i^2} \\ & + \frac{8\Gamma}{R_i}[5G_d^*(\omega) + 2G_m^*(\omega)] + \frac{2\beta_d^*(\omega)}{R_i} \\ & [23G_d^*(\omega) - 16G_m^*(\omega)] + \frac{4\beta_s^*(\omega)}{R_i} \\ & [13G_d^*(\omega) + 8G_m^*(\omega)] \end{aligned} \quad (2)$$

Table 1. Characteristics of PMMA and PS

sample	trademark	$M_w$ (g/mol)	$M_c$ (g/mol)	$M_w/M_n$	$\eta_0$ (Pa s) at 200 °C	$T_g$ (°C)	$E_r$ (kJ/mol)
PMMA	IH830	81,000	10,000	1.8	70,000	116	169.2
PS	GPPS123	215,000	12,000	2.1	5600	97	109.6

$$\begin{aligned}
 D_i = & [2G_d^*(\omega) + 3G_m^*(\omega)][19G_d^*(\omega) + 16G_m^*(\omega)] \\
 & + \frac{48\beta_d^*(\omega)\Gamma}{R_i^2} + \frac{32\beta_s^*(\omega)[\Gamma + \beta_d^*(\omega)]}{R_i^2} \\
 & + \frac{40\Gamma}{R_i}[G_d^*(\omega) + G_m^*(\omega)] + \frac{2\beta_d^*(\omega)}{R_i} \\
 & [23G_d^*(\omega) + 32G_m^*(\omega)] + \frac{4\beta_s^*(\omega)}{R_i} \\
 & [13G_d^*(\omega) + 12G_m^*(\omega)] \quad (3)
 \end{aligned}$$

where  $G_m^*(\omega)$  and  $G_d^*(\omega)$  are the complex shear moduli of the matrix and the dispersed phase, respectively,  $\phi$  is the volume fraction of the dispersed phase,  $\Gamma$  is the interfacial tension,  $R$  is the droplet radius of the dispersed phase, and  $\beta_d^*(\omega)$  and  $\beta_s^*(\omega)$  are the complex interfacial dilatation and interfacial shear modulus, respectively. By fitting the model prediction to experimental data, it is possible to estimate the variation of interfacial tension ( $\Gamma$ ) and interfacial shear modulus ( $\beta_s^*(\omega)$ ) with compatibilizer concentration, and also the interfacial relaxation time ( $\tau_\beta$ ) can be deduced.<sup>28</sup>

Hitherto, most studies on interfacial viscoelasticity of compatibilizers are based on droplet-matrix blends compatibilized with copolymers, while less studies focus on nanoparticles. In general,  $\beta_s^*$  was found to increase with the amount of compatibilizer, while  $\tau_\beta$  was found to reduce with compatibilizer concentration and be dependent on  $\Gamma$ .<sup>14,19</sup> However, these conclusions were drawn based on the prerequisite that compatibilization results in a reduction of interfacial tension and droplet size in a blend system, which undoubtedly affects the Marangoni stresses arising from the nonuniform distribution of compatibilizer on the droplet surface that can relax faster on a smaller droplet.<sup>19</sup>

Apart from the Marangoni stress, interfacial elasticity can also stem from the interfacial films created by compatibilizers, especially when rigid nanoparticles are involved, considering the strong particle–particle interactions and notable caging effects when they are in a crowded or bonded state.<sup>29</sup> That is, at high concentrations, especially above a threshold toward jamming, the diffusional motion of particles is restricted by the overcrowded volume, having particles confined in cages formed by their neighbors. Whether particles escape or not depends on the cage size and degree of jamming. In three-dimensional (3D) colloid systems, the relaxation behavior of particle diffusion can be divided into two parts: movement within the cage and escape from the cage, with the latter being dominant. The phenomenological Vogel–Fulcher–Tammann (VFT) model<sup>30</sup> and the Krieger–Dougherty model<sup>31</sup> are commonly used to describe the exponentially divergent growth of the escape time with particle volume fraction. Excluding particle interactions, the volume fraction in the jammed state or random close packing (RCP) usually lies in the range of 0.5–0.6<sup>32</sup> for 3D geometric packing divergence and 0.8–0.9<sup>33</sup> for 2D. Nevertheless, such jamming contributions at the interface are often neglected in the study of compatibilized blends and are difficult to be explored in light of the

morphology evolution and interfacial tension gradients. So far, to the best of our knowledge, there is no study dedicated to decoupling the contributions of the intrinsic viscoelasticity of interfacial films from that of the Marangoni effect.

Multilayer structures with different polymers alternatively force-assembled via coextrusion or compression have been widely used as model systems<sup>34–39</sup> with well-defined layer numbers and interfacial area to study and quantify the interfacial phenomena encountered in blend systems, with the effects of morphology evolution, surface curvature of the droplet, and interfacial tension gradients readily excluded. However, the interfacial phenomena being focused so far via multilayer studies are other aspects such as interfacial slip<sup>37,40</sup> and interdiffusion,<sup>34,36</sup> with the interfacial rheology of compatibilizers unexplored. Undoubtedly, such model systems will enable the decoupling of the Marangoni effect from the interfacial viscoelasticity of compatibilizers localized at a planar polymer–polymer interface and it is anticipated to obtain a clearer dependence on compatibilizer concentration that solely originates from the interfacial films themselves.

In this study, dumbbell-shaped JNPs composed of PMMA and PS spheres with equal size and crosslink density were synthesized to have a similar affinity to both bulk components in PMMA/PS blends and were studied as a particulate compatibilizer. The blend morphology and the localization of dumbbell JNPs in PMMA/PS blends were assessed to evaluate the compatibilization effect. The linear viscoelasticity of dumbbell JNP-compatibilized PMMA/PS blends was investigated with regard to the effect of composition and JNP concentration, and Palierne model fitting was used to identify the interfacial tension and interfacial shear modulus. More importantly, to decouple the effects of Marangoni stresses and intrinsic viscoelasticity, a sandwiched PMMA/dumbbell JNPs/PS alternating multilayer system was employed for SAOS measurements and compared to the blend systems. The linear viscoelasticity of the multilayer system enabled determination of the interfacial viscoelasticity solely originating from the intrinsic contributions of JNPs residing at the interface (e.g., particle–particle and particle–polymer interactions, etc.). Moreover, a generalized Maxwell model was used to identify the specific contributions of the JNPs including confined diffusion of JNPs within cages and potential entanglements between the crosslinked polymer chains in the JNPs and those penetrating from the bulk phases into the JNPs.

## 2. MATERIALS AND METHODS

**2.1. Materials.** The materials used for the synthesis of JNPs, including sodium dodecylbenzenesulfonate ( $\geq 88.0\%$ ), methyl methacrylate ( $>99\%$ ), potassium persulfate, and divinylbenzene (80%), were purchased from Shanghai Titan Scientific Co., Ltd., except for styrene (St,  $>99\%$ ), which was purchased from Shanghai SECCO Petrochemical Co., Ltd.

The PMMA and PS used for blending are commercial polymers purchased from LG (Korea) Chemical Co., Ltd. and Shanghai SECCO (China) Petrochemical Co., Ltd., respectively. Their characteristics are listed in Table 1. In particular, the entanglement molecular weight ( $M_e$ ) was calculated via  $M_e = \frac{4\rho RT}{5G_N^0}$ , where  $\rho$  is the

density and  $G_N^0$  is the plateau modulus. Considering that the relatively low molecular weight and the not very narrow MWD of the commercial polymers hampered the typical ways of  $G_N^0$  determination (e.g., the terminal peak integration method),  $G_N^0$  was estimated as the ratio of zero-shear viscosity ( $\eta_0$ ) to the number-averaged relaxation time ( $\tau_{0n}$ ) (i.e.,  $G_N^0 = \eta_0/\tau_{0n}$ ).<sup>41</sup> The reciprocal of the frequency corresponding to the cross-over point of the storage ( $G'$ ) and loss ( $G''$ ) moduli curves (Figure S1) was used as  $\tau_{0n}$ , but it should be pointed out that this is only a semi-quantitative method while reasonable for polymers with a not too high polydispersity.<sup>41</sup> The zero-shear viscosity ( $\eta_0$ ) was obtained via Carreau–Yasuda model fitting of the steady state shear curves. The activation energy ( $E_\eta$ ) was obtained from fitting of the Arrhenius law to the temperature dependency of the steady state shear viscosity.

**2.2. Synthesis of PMMA-PS Dumbbell-Shaped JNPs.** The synthesis method of PMMA-PS dumbbell JNPs is given in Supporting Information S2.

### 2.3. Preparation of Blends and Sandwiched Multilayer Structures.

**2.3.1. Preparation of Dumbbell JNPs Compatibilized Blends.** The PMMA/PS blends with various compositions (i.e., 90/10, 80/20, and 50/50 w/w) were prepared by melt blending using a micro twin-screw extruder (SJZS-10B, Wuhan Ruiming Equipment Co. Ltd., China). The added amount of PMMA-PS dumbbell JNPs was varied in the range of 0 to 5 wt % relative to the total amount of PMMA and PS. Prior to blending, the PMMA and PS granules were dried in a vacuum oven at 60 °C for 24 h and then mechanically mixed with the dumbbell JNP powder at a given proportion before being fed into the extruder. Batch melt blending was performed at a processing temperature of 200 °C using a rotation speed of 100 rpm. The extruded strands were cut into small granules and then compression-molded at 200 °C under 10 MPa for 10 min to obtain disks with 25 mm diameter and 1.2 mm thickness. Finally, the disks were annealed in a vacuum oven at 80 °C for 12 h to remove moisture and any residual stress before rheological measurements.

**2.3.2. Preparation of PMMA/JNPs/PS Sandwiched Multilayer Structures.** To fabricate multilayer structures, neat polymer disks (25 mm diameter) with various thicknesses ranging from 100 to 600  $\mu\text{m}$  were prepared via compression molding at 200 °C and 10 MPa for 10 min. Structurally symmetrical multilayer systems with a fixed total thickness of 1.2 mm and a total layer number ranging from 2 to 12 layers were prepared by alternatively stacking PS and PMMA films of identical thickness. Figure 2 shows the schematic diagram of the interfacial structure of the fabricated multilayer disks.

For the multilayer structures with dumbbell JNPs sandwiched at the interface between PS and PMMA layers, 200  $\mu\text{L}$  dispersions of the as-prepared PMMA-PS dumbbell JNPs in ethanol at various concentrations (i.e., 0.1, 0.3, 1, and 3 wt %) were spin-coated (at 300 rpm for 3 min) beforehand onto one side of the PMMA and PS films at room temperature to make sure an identical uniform layer of

JNPs was formed at each interface of the multilayer structures. Figure S3 shows a schematic diagram of the spin-coating process.

**2.4. Rheological Measurements.** Rheological measurements were performed using parallel plates with a diameter of 25 mm and a gap size of 1.2 mm on a stress-controlled rheometer (Discovery HR20, TA Instruments, USA) equipped with an environmental test chamber that was purged with nitrogen during the tests. Time sweeps were performed at 220 °C to test the thermal stability of the samples (Figure S4). Strain sweep tests were conducted to identify the LVE region of the samples for SAOS measurements. Frequency sweep tests were performed at 200 and 220 °C from 100 to 0.01 rad/s with a strain amplitude of 3% lying within the LVE region. Creep tests were performed at 200 and 220 °C, with a shear stress of 50 Pa (a stress pre-determined to be within the linear regime) for 20 min.

**2.5. Morphological Characterization.** To characterize the morphology of PMMA-PS JNPs, the JNPs were ultrasonically dispersed in anhydrous ethanol, deposited on clean carbon-film copper grid and silicon wafer, and air-dried under an ambient atmosphere. The morphology observations were done under transmission electron microscopy (TEM, JEM-2100, JEOL, Japan) and field emission scanning electron microscopy (SEM, Regulus 8100, Hitachi, Japan), and the JNP composition was identified via SEM in combination with energy-dispersive spectrometry (SEM-EDS, Octane election plus, EDAX, USA).

For the blend samples, before the morphology observations under SEM, they were rapidly cryogenically fractured in liquid nitrogen after SAOS rheological testing, and the PS phase in the blend was removed by cyclohexane etching for optimal visualization of the morphological characteristics of the blend. SEM images of the droplet morphology in the blends were analyzed using Image J (Fiji) software<sup>42</sup> to determine the radius of each droplet. Approximately 1000 droplets were considered per sample. Based on the assumption that the droplets are all spherical, the volume average radius ( $R_v$ ) and the number average radius ( $R_n$ ) of the droplets were calculated from discrete radius data derived from SEM images using Python code.

The distribution of JNPs in the blends was observed by TEM and SEM. 100 nm thick sample films were cut at room temperature using an ultramicrotome (Leica EM UC7, Leica Microsystems, Germany) equipped with a diamond knife, and TEM images were obtained at an accelerating voltage of 200 kV. In addition, PMMA/PS 80/20 blends compatibilized by JNPs were treated with PS etching after their SAOS rheological test and observed under SEM with the morphologies of large droplets being selectively focused on and analyzed. Likewise, to determine the interfacial coverage of JNPs in the multilayer systems, after rheological measurement, the PS phase (layers) in the multilayer samples was etched off with cyclohexane to expose the JNPs laden at the interface and the surface morphology of the residual PMMA films was observed under SEM to examine the JNP distributions. The interfacial coverage of JNPs was identified using Image J (Fiji) software.

## 3. RESULTS AND DISCUSSIONS

### 3.1. Morphology and Janus Character of Dumbbell-Shaped JNPs.

The morphology of the as-synthesized PMMA-PS dumbbell JNPs was observed under SEM and TEM, and the corresponding images of representative JNPs are shown in Figure 3a,b. As expected, all the JNPs show a dumbbell shape with two spherical nanoparticles linked together and the diameter of the nanoparticles on each side is almost equal,  $\sim 80$  nm, while the size along the long axis of a single intact JNP is approximately 150 nm. The SEM-EDS mapping analysis based on one specific JNP in Figure 3a shows that the C element (Figure 3c) is homogeneously distributed over the whole JNP, which is due to the fact that both PS and PMMA have a C-based main chain structure. However, the O element (Figure 3d), solely existing in the ester groups of PMMA, was observed to concentrate only in one spherical side of the JNP, thereby confirming that to be the PMMA sphere. Undoubtedly, the

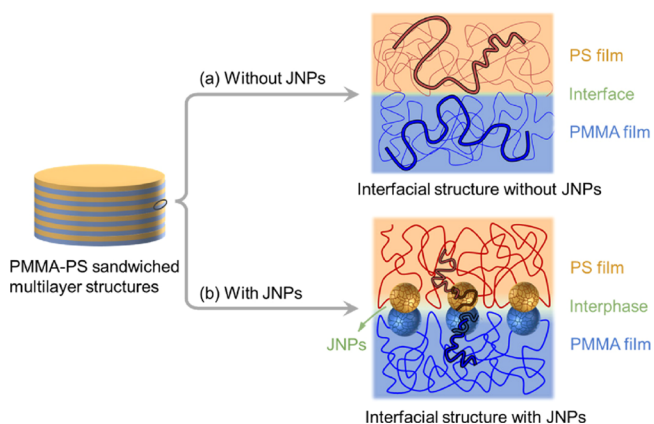


**Figure 2.** Schematic illustration of the interface between sandwiched multilayer structures (a) without and (b) with JNPs.

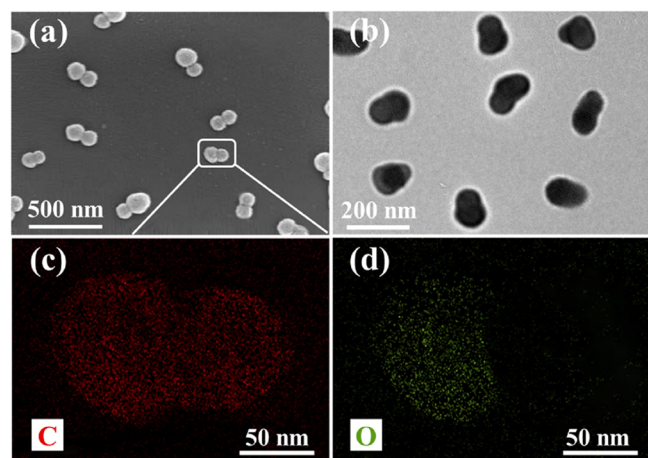


**Figure 3.** (a) SEM and (b) TEM images of dumbbell-shaped PMMA-PS JNPs; SEM-EDS elemental maps of (c) C and (d) O of a single JNP based on (a).

SEM, TEM, and EDS analyses confirm the successful synthesis of dumbbell-shaped PMMA-PS JNPs and demonstrate their chemical asymmetry. The FTIR spectra, showing characteristics of both PS and PMMA, further confirm the successful synthesis of dumbbell-shaped JNPs and are shown in Figure S5.

**3.2. Compatibilization Effect in Blends.** **3.2.1. Morphology Refinement in both Droplet-Matrix and Co-Continuous Blends.** The as-synthesized PMMA-PS dumbbell JNPs were expected to locate at the interface between the PS and PMMA phases and to act as a compatibilizer. The compatibilization effect can be confirmed from morphology refinement of the dispersed domains in the blend. PMMA/PS blends with various compositions and JNP contents were prepared, and their morphology, with the PS phase selectively etched out, was observed under SEM. Figure 4 shows SEM graphs of PMMA/PS 80/20 and 50/50 blends with various amounts of JNPs. As can be seen, the 80/20 blend has a typical droplet-matrix morphology, with PS being the dispersed phase, while the morphology of 50/50 blends are co-continuous. Being filled with JNPs, both the droplet-matrix and the co-continuous morphologies experienced a structural refinement with reduced domain size, confirming the compatibilization

effect of the JNPs. In particular, as listed in Table 2, the volume average radius ( $R_v$ ) of droplets in the 80/20 blend decreased

**Table 2. Volume Average Radius ( $R_v$ ), Number Average Radius ( $R_n$ ), and Polydispersity ( $R_v/R_n$ ) of the Dispersed Phase of PMMA/PS 80/20 Blends**

sample	$R_v$ ( $\mu\text{m}$ )	$R_n$ ( $\mu\text{m}$ )	$R_v/R_n$
80/20	0.74	0.42	1.7
80/20/0.5	0.62	0.33	1.9
80/20/1	0.54	0.26	2.1
80/20/1.5	0.48	0.22	2.2
80/20/2	0.45	0.20	2.2
80/20/2.5	0.43	0.19	2.3

from 0.74 to 0.43  $\mu\text{m}$ , as the concentration of JNPs was increased from 0 to 2.5 wt %, and the distribution of droplet sizes, in terms of  $R_v/R_n$  ratios, became wider. Such a compatibilization effect is consistent with earlier studies that reported the use of JNPs assembled from an ABC triblock terpolymer<sup>43</sup> and of Janus hybrid silica/polymer nanoparticles<sup>44</sup> in enhancing compatibilization in polymer blends.

**3.2.2. Localization of JNPs at the Interface.** It is generally known that the compatibilization efficiency of a compatibilizer strongly depends on its preference to be localized at the interface.<sup>4,8,45</sup> After the frequency sweep tests, the PMMA/PS 80/20 blends were subjected to PS phase etching and were then observed under high-magnification SEM to examine the localization of the JNPs in the blends; the images are shown in Figure 5. As expected, the JNPs were almost completely located at the PMMA/PS interface, with dense patches of JNPs coating the PS droplet interfaces visible in Figure 5, while only a negligibly small fraction is present in the PMMA matrix. This clearly demonstrates that the dumbbell JNPs exhibit an excellent interfacial activity to be efficiently driven to the interface, having the PS and PMMA spheres of the dumbbell potentially penetrating into the droplet and the matrix, respectively. Note that since the PS spheres were crosslinked, they were unaffected during the etching of the PS droplet and thus the complete JNPs remained observable. Moreover, as the amount of JNPs was increased, more JNPs were observed at the interface with a denser packing density while still in the form of a monolayer coverage. Such a monolayer consisting of JNPs jamming at the interface undoubtedly plays a key role in

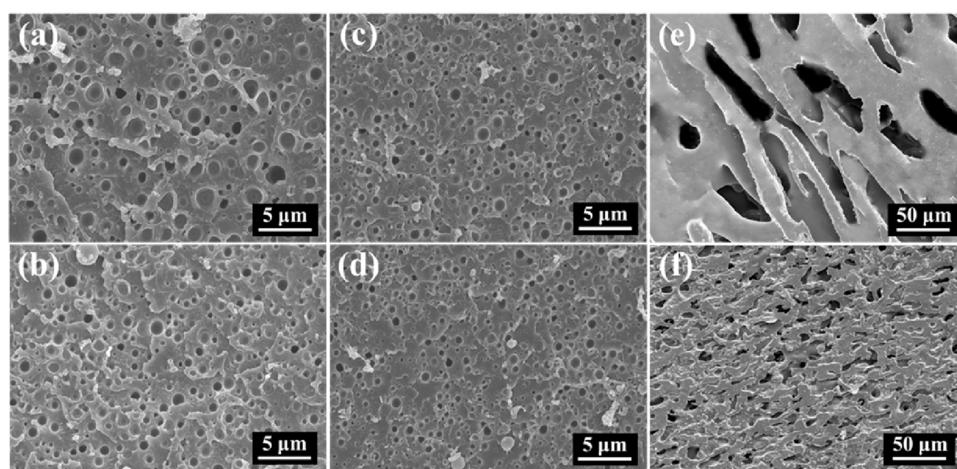


**Figure 4.** SEM micrographs of (a) 80/20, (b) 80/20/1, (c) 80/20/2, (d) 80/20/2.5, (e) 50/50, and (f) 50/50/5 blends after etching PS.

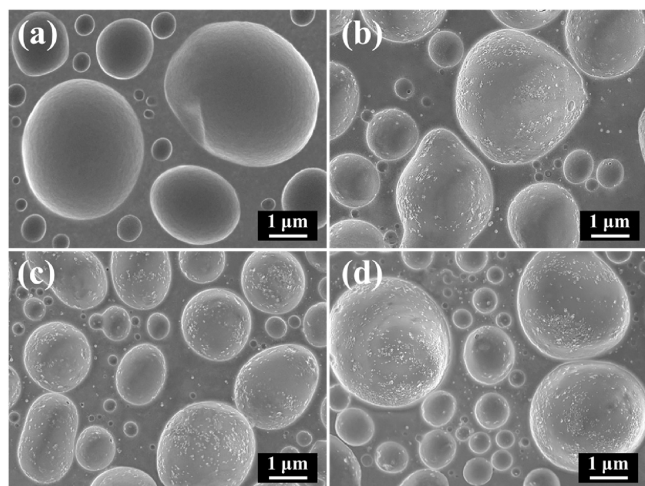


**Figure 5.** High-magnification SEM micrographs of some particularly selected large droplets to show the localization of JNPs based on 80/20 blends after the frequency sweep test and PS phase etching with various JNPs concentrations: (a) 0%, (b) 1%, (c) 2%, and (d) 2.5%.

suppressing coarsening and stabilizing the refined morphology, as confirmed by the reduced domain size with increased JNP concentration shown in Figure 4. It is worthwhile to note that the droplets in Figure 5 are some extremely large droplets being particularly selected from each sample to facilitate the observation of JNPs on the droplet surface. Hence, direct comparison of the droplet size between different images in Figure 5 is not relevant. In addition, JNPs located on the surface of the small droplets can also be observed if the images are magnified.

To further verify the localization and distribution of JNPs at the PMMA/PS interface, after the frequency sweep test, the PMMA/PS (80/20) blends loaded with various concentrations of JNPs were also subjected to TEM characterization. As shown in Figure 6, a clear droplet-matrix morphology was demonstrated, with the gray phase and the black phase in the TEM images being the PMMA matrix and PS domains, respectively. However, since the JNPs (see Figure 3b) were composed of PMMA and PS, being the same materials as the bulk polymers that can exhibit similar contrast under TEM, it is very difficult to clearly identify the morphology of the dumbbell-shaped JNPs at the PMMA/PS interface. Nonetheless, as shown in Figure 6, different from the purely black droplets in the neat blend (Figure 6a), a gray and black periphery (denoted by the red lines) is clearly observable in the blend samples loaded with the JNPs (Figure 6b–d), which is believed to be a layer of JNPs anchoring at the PMMA/PS interface. Moreover, as the amount of JNPs was increased, the gray-black periphery became more pronounced, confirming an increased packing density of the JNPs at the interface. Meanwhile, the domain size was also observed to reduce with increased JNP concentration, confirming again the key role of the JNPs jamming at the interface in suppressing coarsening and stabilizing the refined morphology. Note that from the TEM images, the JNPs were nearly unobserved in the bulk.

In general, the interface does not need to be fully saturated with compatibilizer; only a certain surface coverage is sufficient to inhibit droplet coalescence.<sup>12,15,46</sup> To better understand the compatibilization effect, it is crucial to determine the surface coverage of JNPs at the droplet interface ( $\Sigma$ ). Assuming that

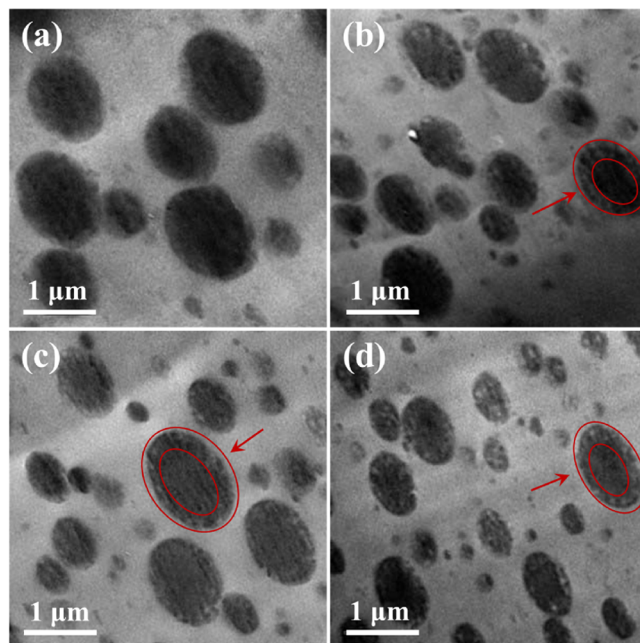


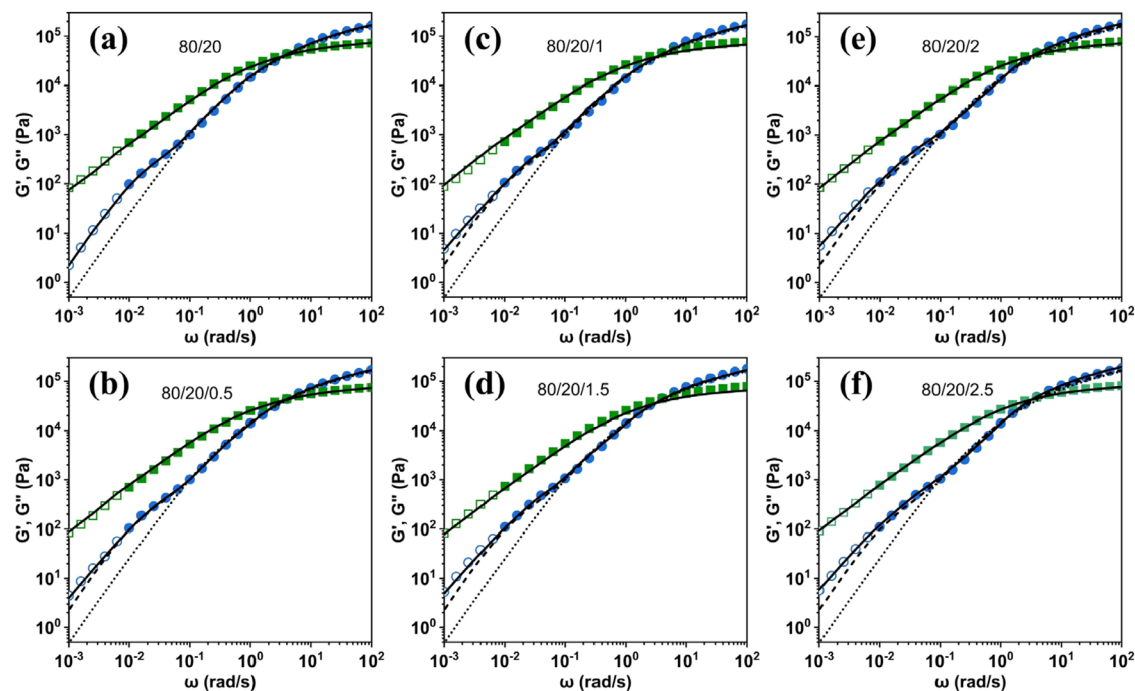
**Figure 6.** TEM images of PMMA/PS (80/20) blends after the frequency sweep test with various JNP concentrations: (a) 0%, (b) 1%, (c) 2%, and (d) 2.5%. The red lines are to guide the eye.

the droplets are spherical, that the JNPs are all located at the interface, and that the coverage of a single JNP equates its maximum cross-section area (i.e., the equatorial area of the side sphere), the  $\Sigma$  (i.e.,  $\Sigma_{\text{theory}}$ ) can be theoretically estimated based on the  $R_v$  and ingredient ratio shown in Table 2. The  $\Sigma_{\text{theory}}$  values were calculated to be  $\sim 5.5$ ,  $\sim 8.4$ , and  $\sim 10.1\%$  for JNP concentrations ( $w_{\text{JNPs}}$ ) of 1, 2, and 2.5 wt %, respectively. Likewise, the  $\Sigma$  can be experimentally determined ( $\Sigma_{\text{exp}}$ ) using Image J (Fiji) software based on the JNPs localized at the droplet interface, as shown in Figure 5, which resulted in surface coverage values of  $\sim (5.9 \pm 0.1)\%$ ,  $\sim (8.3 \pm 0.4)\%$ , and  $\sim (9.7 \pm 0.6)\%$  for  $w_{\text{JNPs}} = 1, 2,$  and  $2.5$  wt %, respectively. The  $\Sigma_{\text{exp}}$  and  $\Sigma_{\text{theory}}$  are very consistent with each other considering the assumptions. Moreover, as shown in Table 2, for 80/20 blends, the droplet size reduction with  $w_{\text{JNPs}}$  is substantial when the JNP concentration is less than 2 wt %, whereas it is nearly saturated when the  $w_{\text{JNPs}}$  is above 2 wt %. This indicates that a surface coverage  $\Sigma \sim 10\%$  is sufficient to largely resist droplet coalescence and reach a saturated domain size refinement.

In fact, since the Janus particle size is comparable to the droplet radius due to the interfacial curvature effect, it is likely that the inner parts of the JNPs in the droplet jam at a lower particle concentration. An effective interfacial coverage ( $\Sigma_{\text{effective}}$ ) should thus be defined. For this, You and Yu<sup>47</sup> proposed the concept of curvature radius of the jamming regime ( $R_{\text{jamming}}$ ) based on the touching of the inner parts of the Janus particles to take into account the geometric confining effect. For our case of dumbbell-shaped JNPs with symmetric PMMA and PS spheres that have similar affinities to both bulk matrices, the JNPs can symmetrically distribute at the interface (Figure 1), and the  $R_{\text{jamming}}$  can be determined as  $R_{\text{jamming}} = R_v - R_{\text{particle}}$ , where  $R_v$  is the volume average radius of the dispersed phase droplet, and  $R_{\text{particle}}$  is the radius (40 nm) of the PS sphere part of the dumbbell-shaped JNP. Based on the  $R_{\text{jamming}}$ , the interfacial coverage of the jammed state ( $\Sigma_{\text{jamming}}$ )

**Table 3.** Key Parameters Regarding the Interfacial Coverage of PMMA/PS 80/20 Blends Loaded with Various Concentrations of the Dumbbell-Typed JNPs

sample	$\Sigma_{\text{theory}}$ (%)	$\Sigma_{\text{exp}}$ (%)	$R_{\text{jamming}}$ ( $\mu\text{m}$ )	$\Sigma_{\text{jamming}}$ (%)	$\Sigma_{\text{effective}}$ (%)
80/20/1	5.5	$5.9 \pm 0.1$	0.50	65.2	$7.8 \pm 0.2$
80/20/2	8.4	$8.3 \pm 0.4$	0.41	63.1	$13.6 \pm 0.6$
80/20/2.5	10.1	$9.7 \pm 0.6$	0.39	62.5	$15.7 \pm 0.6$

**Figure 7.** Storage moduli ( $G'$ ) (circles) and loss moduli ( $G''$ ) (squares) at 200 °C compared to Palierne model predictions for PMMA/PS 80/20 blends with various amounts of JNPs: (a) 0 wt %; (b) 0.5 wt %; (c) 1 wt %; (d) 1.5 wt %; (e) 2 wt %; and (f) 2.5 wt %. The solid symbols are the results from frequency sweep tests, and the hollow symbols are the converted data from creep tests. The full line is the fitting result of the Palierne model. The dotted line is the contribution of the blend components at  $\Gamma = 0$  based on Kerner's model (eq 4). The dashed line is the contribution of the blend components and interface at  $\beta_d = 0$  and  $\beta_s = 0$ .

was defined as the product of the packing density of the jammed state (0.76)<sup>48</sup> with the ratio of the available area at  $R_{\text{jamming}}$  versus the interfacial area,<sup>47</sup> that is,  $\Sigma_{\text{jamming}} = 0.76 \times (R_{\text{jamming}}^2/R_v^2)$ . Subsequently, the ratio of the experimentally determined interfacial coverage to the jamming interfacial coverage can be described as the effective interfacial coverage ( $\Sigma_{\text{effective}}$ ):  $\Sigma_{\text{effective}} = \Sigma_{\text{exp}}/\Sigma_{\text{jamming}}$ . The calculated data based on PMMA/PS 80/20 blends loaded with various concentrations of JNPs are given in Table 3. As expected, the JNPs required a much lower interfacial coverage to reach jamming ( $\Sigma_{\text{jamming}}$ ) than the typical threshold value of 0.76. The  $\Sigma_{\text{jamming}}$  was further reduced with increased JNP concentration as a result of the reduced droplet size. Likewise, the effective interfacial coverage ( $\Sigma_{\text{effective}}$ ) is much higher than the value determined from particles covered at the droplet surface and significantly increased with the JNP concentration. This discussion provides additional quantitative evidences on the enhanced stabilization role of the dumbbell-typed JNPs in refining the phase domain size due to its additional geometric confinement effect.

**3.2.3. Linear Viscoelasticity.** Figure 7 shows the frequency dependency of the storage ( $G'$ ) and loss ( $G''$ ) moduli of PMMA/PS 80/20 blends that have a typical droplet-matrix morphology. To obtain a broad frequency window to capture the characteristic relaxations, both SAOS measurements and

creep tests were performed for each sample and the creep data were transformed into dynamic moduli using the Schwarzl method<sup>49</sup> to extend the window to a lower frequency range, as done in earlier studies.<sup>50,51</sup> Unless otherwise indicated, the dynamic moduli curves shown in the current study are a superposition of SAOS and creep data. As can be seen in Figure 7, it is clear that in the blends, an enhanced elasticity with a distinct  $G'$  shoulder occurs in the low frequency region (c.a.  $10^{-2}$  to  $10^{-1}$  rad/s), indicating the shape relaxation of the dispersed droplets, in agreement with earlier studies on blends with a droplet-matrix morphology.<sup>21,52–54</sup> For the blends filled with JNPs, the  $G'$  curve demonstrates a subtle increment in the terminal region as compared to that of the pure 80/20 blend (the dashed line) (see Figure 7b–d). This subtle difference is believed to be a contribution of the interfacial viscoelasticity of the JNPs laden at the interface. This is widely reported for block copolymer-compatible blends while rarely reported for nanoparticles compatibilized blends.<sup>9,14</sup>

The Palierne emulsion model that has been extensively demonstrated to be effective in describing the LVE behavior of incompatible blends with droplet-matrix morphologies<sup>20,55–57</sup> is used here to evaluate the compatibilization effect of the dumbbell JNPs. Both the generalized version of the Palierne model<sup>19</sup> that takes into account the interfacial tension ( $\Gamma$ ) and interfacial shear modulus ( $\beta_s$ ) and the Kerner's version<sup>58,59</sup>

that considers only the component contributions assuming  $\Gamma = 0$  are used to fit the LVE data of the blends. The Kerner model expressed in term of complex modulus is as follows

$$G^*(\omega) = G_m^*(\omega) \frac{[2G_d^*(\omega) + 3G_m^*(\omega)] + 3\phi[G_d^*(\omega) - G_m^*(\omega)]}{[2G_d^*(\omega) + 3G_m^*(\omega)] - 2\phi[G_d^*(\omega) - G_m^*(\omega)]} \quad (4)$$

where  $G^*(\omega)$ ,  $G_m^*(\omega)$ , and  $G_d^*(\omega)$  are the complex moduli of the blend, the matrix, and the dispersed phase, respectively. As shown in Figure 7, the Kerner model fits the high frequency region well, whereas it fails to capture the shape relaxation shoulder in the low frequency region, thereby demonstrating the importance of considering the interfacial tension for describing the droplet shape relaxation. In contrast, the generalized Palierne model using  $\Gamma$  and  $\beta_s$  as fitting parameters, with  $\beta_d$  assumed to be negligible, as in previous studies,<sup>19–21</sup> describes the dynamic moduli of the uncompatibilized and compatibilized blends well over the whole frequency range. The fitting parameters are listed in Table 4. This good fitting

**Table 4. Interfacial Tension and Interfacial Shear Modulus of PMMA/PS 80/20 Blends Obtained from the Palierne Model Fitting of the Linear Viscoelastic Data (eqs 1–3)**

sample	$\Gamma$ (mN/m)	$\beta_s$ (mN/m)
80/20/0	1.23	
80/20/0.5	0.92	0.288
80/20/1	0.72	0.344
80/20/1.5	0.59	0.404
80/20/2	0.55	0.502
80/20/2.5	0.53	0.568

result confirms that the linear viscoelasticity of JNP-compatibilized blends consists of the contributions from the polymer components, the droplet shape relaxation, and the interfacial relaxation of the JNPs.

Note that it might be argued that the deviation of  $G'$  from the prediction of the simplified Palierne model omitting the  $\beta_s$  item (dashed line) in the terminal zone (i.e., at low frequencies) (Figure 7) is due to the polydispersity of droplet size ( $R_v/R_n$ ) instead of the interfacial relaxation of the JNPs. In fact, as reported by Graebing et al.,<sup>21</sup> the effect of droplet polydispersity on the Palierne model prediction for the secondary plateau is very limited if the polydispersity does not exceed 2.3, as is the case in the current study (Table 2). Moreover, the effect of polydispersity often results in a less well-defined secondary plateau and a lower strength of the shape relaxation in Cole–Cole plots. In this work, an enhanced strength of the shape relaxation in Cole–Cole plots (Figure S6) together with the emergence of an evident third relaxation was observed in the blends with JNPs, thereby excluding the effect of droplet polydispersity but rather indicating a contribution of the interfacial relaxation.

The interfacial tension ( $\Gamma$ ) was determined from the Palierne model fitting parameter  $\Gamma/R_v$ , using the  $R_v$  values in Table 2. For the uncompatibilized PMMA/PS blend, the thus obtained value is 1.23 mN/m, which is consistent with the values reported in literature,<sup>60</sup> which are in the range 1.2–2.5 mN/m. Moreover, as shown in Table 4, the  $\Gamma$  decreases with increasing amounts of JNPs, reaching a value of 0.53 mN/m when the added amount is 2.5 wt %. This confirms the

excellent compatibilization efficiency of the PMMA-PS dumbbell JNPs, which is expected to originate from the dumbbells being preferentially located at the interface, considering that both the PS and PMMA spheres in a dumbbell have a good affinity to the PS and PMMA bulk phases, respectively, hence endowing the JNP dumbbells with an excellent surfactant-like surface activity.

The interfacial tension reduction as a function of JNP concentration can be described by an exponential function that was used in earlier studies<sup>61</sup> to describe the effect of compatibilizer concentration

$$\Gamma = (\Gamma_0 - \Gamma_s)e^{-k_1 w} + \Gamma_s \quad (5)$$

where  $\Gamma_0$  and  $\Gamma_s$  are the interfacial tension values of blends with no compatibilizer and with a saturated amount of compatibilizer, respectively;  $w$  is the concentration of compatibilizer; and  $k_1$  represents an intrinsic parameter describing the sensitivity of interfacial tension to compatibilizer content. In the limit of  $w \rightarrow \infty$ , eq 5 becomes

$$\lim_{w \rightarrow \infty} \Gamma = \lim_{w \rightarrow \infty} [(\Gamma_0 - \Gamma_s)e^{-k_1 w} + \Gamma_s] = \Gamma_s \quad (6)$$

where  $\Gamma_s$  is the minimum  $\Gamma$  that can be achieved with compatibilizer (here, the JNPs). The fitting results of eq 5 are given in Figure 8a. For comparison, the data of PMMA-*ran*-PS

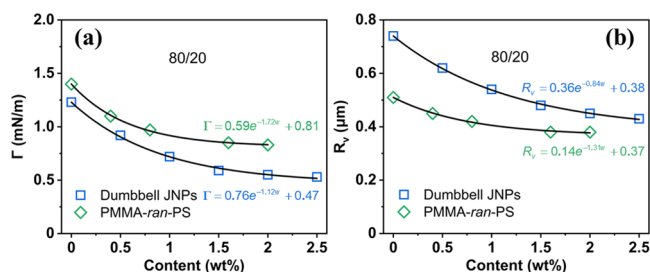


**Figure 8.**  $\Gamma$  and  $R_v$  of PMMA/PS 80/20 blends as a function of JNPs and PMMA-*ran*-PS concentration. The results for PMMA-*ran*-PS are extracted from ref 62. The lines are the fitting result of eqs 5 and 8.

compatibilized blends extracted from the results of Yee et al.<sup>62</sup> are also plotted. As shown in Figure 8a, the model fitting is good for both the JNPs and the PMMA-*ran*-PS systems with  $k_1 = 1.12$  and 1.72 and  $\Gamma_s = 0.47$  and 0.81 mN/m, respectively. The larger difference between  $\Gamma_0$  and  $\Gamma_s$  of the JNPs as compared to the PMMA-*ran*-PS indicates a better compatibilization efficiency of the PMMA-PS dumbbell JNPs, though its  $k$  value is slightly smaller than that of the copolymer. The smaller  $k$  value is reasonable, considering that for the same concentration (wt %), the bigger and slightly denser JNPs may occupy less area at the interface. The fact that the difference in concentration ( $w_{\text{JNPs}} \approx 2.5$  wt %) to reach the saturated  $\Gamma$  is minor, despite a factor of about 10 difference in size of the JNPs versus a copolymer molecule ( $R_g \sim 12.7$  nm), also confirms the excellent interfacial localization and activity of the JNPs. Moreover, to link the compatibilization more directly to the anchoring of the particles at the interface, the effective interfacial coverage ( $\Sigma_{\text{effective}}$ ) was also used to replace the  $w_{\text{JNPs}}$  in eq 5 to describe the dependence of the interfacial tension as a function of  $\Sigma_{\text{effective}}$  (Figure S7). A lower  $\Gamma_s$  of 0.43 mN/m was obtained from the fitting as compared to that of 0.47 mN/m from the dependence on  $w_{\text{JNPs}}$ , but the difference is minor

when compared to the initial interfacial tension (1.23 mN/m) of the uncompatibilized blends.

In addition, in view of the close relation between morphology refinement and interfacial tension via<sup>63</sup>

$$D = \frac{4\Gamma p^{\pm 0.84}}{\dot{\gamma} \eta_m} \quad (7)$$

where  $D$  is the droplet diameter,  $p$  is the viscosity ratio ( $\eta_d/\eta_m$ ) (positive exponents for  $p > 1$ , while negative values for  $p < 1$ ),  $\dot{\gamma}$  is the shear rate, and  $\eta_m$  is the matrix viscosity; one can obtain a similar relationship between droplet radius and compatibilizer concentration for a given system subjected to the same shear conditions. The relation is as follows<sup>61</sup>

$$R_v = (R_{v0} - R_{vs})e^{-k_2 w} + R_{vs} \quad (8)$$

where  $k_2$  is the parameter that governs droplet radius variation with compatibilizer concentration,  $R_{v0}$  and  $R_{vs}$  are the average droplet radius of the dispersed phase with no compatibilizer and with a saturated amount of compatibilizer, respectively. As shown in Figure 8b, the droplet radius decreases with compatibilizer concentration with a trend similar to that of the interfacial tension, being well fitted by eq 8 with  $k_2 = 0.84$  and 1.31 and  $R_{vs} = 0.38$  and  $0.37 \mu\text{m}$  for PMMA-PS dumbbell JNPs and PMMA-*ran*-PS copolymer, respectively. A similar trend was also reported in SiO<sub>2</sub>-based JNPs compatibilized poly(vinylidene fluoride) (PVDF)/poly(lactic acid) (PLLA) blends by Wang et al.<sup>64</sup> Likewise, the large droplet radius ( $R_v$ ) reduction, that is, 39% reduction (from 0.74 to 0.45  $\mu\text{m}$ ) with 2 wt % dumbbell JNPs as compared to the 25% reduction (from 0.51 to 0.38  $\mu\text{m}$ ) with 2 wt % PMMA-*ran*-PS copolymer<sup>62</sup> again verifies a better compatibilization efficiency of the JNPs over the copolymer. Note that the reference size of the neat droplets is related to the material characteristics (e.g., molecular weight, viscosity ratio, and interfacial tension) and processing conditions (e.g., temperature, mixing time, and shear rate),<sup>53,65,66</sup> which can be different between both studies.

As shown in Table 4, the interfacial modulus  $\beta_s$  is increasing with JNP concentration from 0.288 mN/m in 80/20/0.5 to 0.568 mN/m in 80/20/2.5. This confirms the substantial interfacial elasticity contributed by the JNPs at the interface, which is consistent with observations in clay-compatibilized blends<sup>14</sup> and in silica/polystyrene Janus hybrid nanoparticle-compatibilized blends.<sup>9</sup> Such a high interfacial elasticity as a result of the JNPs Pickering effect is crucial in resisting droplet coalescence.

**3.3. Interfacial Rheology of JNP-Covered Interfaces: Polymer Blends Versus Multilayer Structures.** **3.3.1. Interfacial Relaxation Behavior in Blends.** As shown in Figure 7, a droplet shape relaxation ( $\tau_F$ ) shoulder can be detected in the  $G'$  curves in the low frequency region for uncompatibilized PMMA/PS blends. When JNPs are added, an additional interfacial relaxation ( $\tau_\beta$ ) shoulder is observed at frequencies corresponding to timescales longer than  $\tau_F$ . Since the weighted relaxation spectrum,  $(H(\tau)*\tau)$ , is very sensitive to distinguish relaxation behaviors, the  $(H(\tau)*\tau)$  spectra of the PMMA/PS blends and the neat polymers are calculated from frequency-dependent data according to a nonlinear regularization method proposed by Honerkamp and Weese<sup>67</sup> (see eq 9).

$$H(\tau) = G' \left[ \frac{d \log G'}{d \log \omega} - \frac{1}{2} \left( \frac{d \log G'}{d \log \omega} \right)^2 - \frac{1}{4.606} \frac{d^2 \log G'}{d (\log \omega)^2} \right]_{\tau = \sqrt{2}/\omega} \quad (9)$$

Figure 9 shows the storage moduli and the weighted relaxation spectra of PMMA/PS blends with various

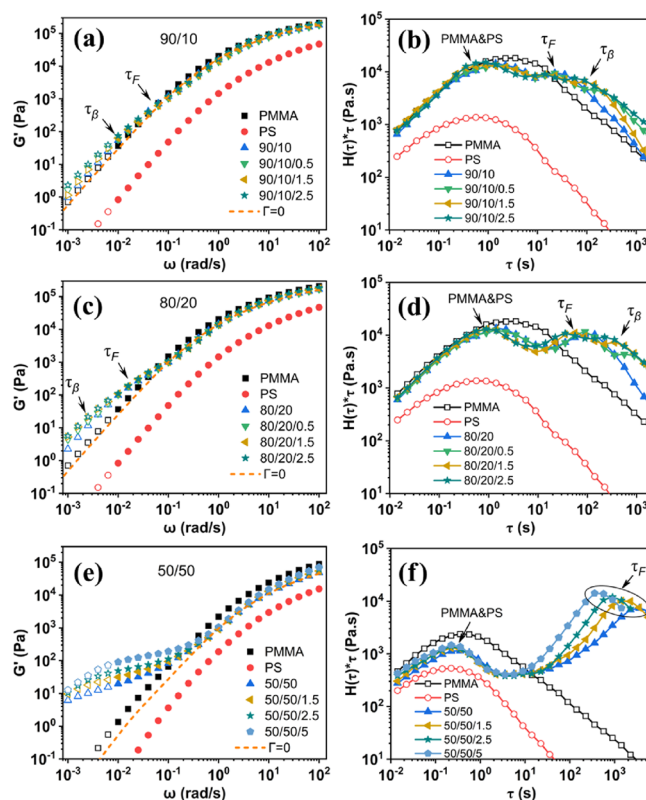


**Figure 9.** (a,c,e) Storage moduli and (b,d,f) relaxation spectra of PMMA/PS 90/10 and 80/20 blends at 200 °C and 50/50 blends at 220 °C with various JNPs amounts. The solid symbols are the results from dynamic tests, and the hollow symbols are the conversion data from creep tests. The dashed line is the contribution of the blend components at  $\Gamma = 0$  based on Kerner's model (eq 4).

compositions (90/10, 80/20, and 50/50) and various JNP concentrations. Additional storage moduli and relaxation spectra of the 80/20 and 90/10 blends with 1 and 2 wt % JNPs concentrations are presented in Figure S8. The blends with 90/10 and 80/20 composition have droplet-matrix morphologies, whereas the 50/50 blend has a co-continuous morphology. As can be seen, the characteristic relaxations are dependent on blend composition and JNP concentration, more specifically, on the morphology of the dispersed phase. In the relaxation spectra, the uncompatibilized blends are characterized by two maxima, one corresponding to the fast relaxation of the polymers (PMMA and PS overlapped) and the other to the much slower shape relaxation ( $\tau_F$ ). As the PS (minor phase) fraction is increased (its domain size increased correspondingly), the  $G'$  shoulder of  $\tau_F$  in the terminal region becomes more pronounced and  $\tau_F$  shifts toward a longer time. This is particularly remarkable when the PS fraction is increased to form a co-continuous morphology (i.e., 50/50

blend), where the significant elasticity enhancement of  $\tau_F$  is featured by a power-law relationship ( $G' \sim \omega^n$ ) (Figure 9e) instead of a shoulder, in agreement with literature.<sup>23</sup> It is worth noticing that for 50/50 blends, the peak of the shape relaxation was not accessible at 200 °C within the measurement range ( $<10^3$  s) of the relaxation time spectrum (see Figure S9b). Hence, experimental data obtained at 220 °C with an accelerated relaxation process are used for discussion (Figure 9e).

The observation of a shape relaxation peak for co-continuous structures was rarely reported in the literature but indeed anticipated by Yu et al.<sup>23</sup> to occur at very low frequencies. More often, it was partially observed as a tail in the weighted relaxation spectrum similar to the one shown in Figure S9b and, as mentioned above, characterized with a power-law dependency of  $G'$  on  $\omega$  within a broad range of timescales in the terminal region. Such a characteristic was attributed by Li et al.<sup>68</sup> to the structural relaxation of interpenetrating co-continuous networks, by Weis et al.<sup>69</sup> to the existence of domains of different characteristic lengths and by López-Barrón and Macosko<sup>3,70,71</sup> to the distribution of local shape and size of the co-continuous interface having various interfacial areas and interfacial curvatures. In summary, the increased elasticity with longer relaxation times with a broader distribution for co-continuous blends in SAOS can also be considered as a shape relaxation of the co-continuous phases with varied length scales, however being slightly different from droplet shape relaxations of droplet-matrix blends that result in shorter relaxation times with a narrower distribution.

As far as the addition of JNPs is concerned, it is very clear from both the  $G'$  curves and the relaxation spectra of 90/10 and 80/20 blends (Figure 9a–d) that apart from the combined relaxation of PMMA and PS chains and the shape relaxation ( $\tau_F$ ) of the dispersed droplets, an additional relaxation is present at a longer time than  $\tau_F$ . This additional relaxation can most likely be attributed to the interfaces laden with JNPs and is thus named the interfacial relaxation ( $\tau_\beta$ ). In our case of PMMA-PS dumbbell JNPs at the interface between the PMMA and PS phases, the interfacial contributions can be threefold. First, the JNPs on the interface can exhibit clustering and network formation, thereby reaching a jammed state, which creates a robust film at the interface that can account for a key contribution to the interfacial viscoelasticity. Second, a Marangoni stress arising from the redistribution of JNPs at the droplet interface due to the applied shear flow field (see Figure 1) can provide a major contribution. Third, for polymeric JNPs dispersed in melts of the same polymer (i.e., the PMMA sphere in the PMMA bulk and the PS sphere in the PS bulk), polymer chains in the bulk likely penetrate into the JNPs and establish entanglements with the crosslinked chains in the JNPs (see Figure 11a shown below), thereby significantly contributing to a good interfacial adhesion and interfacial viscoelasticity.

However, in co-continuous systems (i.e., 50/50 blend) compatibilized with JNPs, the  $\tau_\beta$  is not observed (see Figure 9e,f). This is most likely because  $\tau_\beta$  occurs at a very long time, far beyond the experimental measurement window. Despite this, the effect of JNPs on 50/50 blends is very striking in shortening the  $\tau_F$  value and its corresponding power-law plateau in the  $G'$  curve, while increasing the height of the relaxation peak in the  $(H(\tau)*\tau)$  spectra. This can be explained by the morphological changes observed in the SEM images of the blend (Figure 4e,f). The addition of JNPs caused a morphological refinement and hence induced a faster

relaxation of the co-continuous structure. To our knowledge, this is the first time that an accelerated shape relaxation of a co-continuous structure is being reported as a result of compatibilization by JNPs, though a similar observation has been reported by López-Barrón and Macosko<sup>3</sup> on co-continuous blends refined by block copolymers. As mentioned above, a similar but less significant effect of the JNPs on the  $\tau_F$  is also observed in the droplet-matrix blends as a result of domain size reduction (Figure 9b,d).

The shape ( $\tau_F$ ) and interfacial ( $\tau_\beta$ ) relaxation times of the blends are plotted versus JNP concentration ( $w_{\text{JNPs}}$ ) in Figure 10 and are fitted to a power-law equation as follows<sup>26</sup>

$$\tau_F \ \& \ \tau_\beta \propto w^{-k_\tau} \quad (10)$$

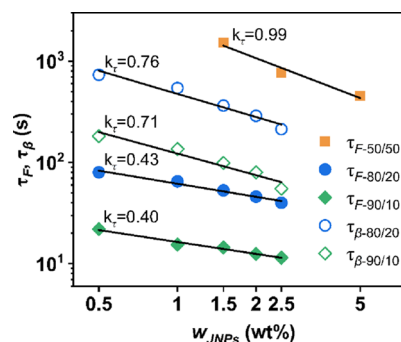


**Figure 10.** JNP concentration ( $w_{\text{JNPs}}$ ) dependence of relaxation times  $\tau_F$  and  $\tau_\beta$  for 50/50, 80/20, and 90/10 blends. The solid line corresponds to the linear regression of eq 10.

Note that the relaxation times for 50/50 blends (i.e.,  $\tau_F$ ) were collected at 220 °C, and those for 80/20 and 90/10 blends (i.e.,  $\tau_F$  and  $\tau_\beta$ ) at 200 °C. As shown in Figure 9, the reduction of  $\tau_F$  and  $\tau_\beta$  with decreasing minor phase (PS) fraction is significant as a result of the refined droplet morphology, with  $\tau_F$  of the 50/50 blend being several orders of magnitude higher than that of the 80/20 and 90/10 blends; the latter differ only by one order of magnitude. Moreover, when the blends are compatibilized with dumbbell JNPs, both  $\tau_F$  and  $\tau_\beta$  decrease with  $w$ , having a quite similar exponent ( $\sim 0.40$  for  $\tau_F$  and  $\sim 0.71$  for  $\tau_\beta$ ) for droplet-matrix blends, while a higher value (i.e.,  $k_\tau \sim 0.99$  for  $\tau_F$ ) is obtained for the co-continuous blend. Undoubtedly, these reductions are related to the morphology refinement of the droplets and the co-continuous phase domains as a result of compatibilization, which was also reported in the case of block copolymer-compatibilized PMMA/PS blends.<sup>26</sup> Smaller droplets naturally exhibit a faster shape relaxation and additionally facilitate fast relaxation of JNP concentration gradients due to the lower distance over which these gradients can spread out.<sup>20</sup> Also, a higher JNP coverage of the interface accelerates the rearrangement of the JNP distribution over the droplet surface (i.e., Marangoni stress relaxation at the interface) resulting in a shorter  $\tau_\beta$ . In summary, in blend systems, the JNP concentration dependence of  $\tau_F$  and  $\tau_\beta$  is clearly dominated by the morphology evolution and the Marangoni stress effect, hampering the determination of the intrinsic interfacial viscoelasticity of the JNPs film at the interface.

It is worth noting that in addition to the time shift of  $\tau_F$  and  $\tau_\beta$ , the height of the relaxation peaks (especially that of  $\tau_\beta$ )

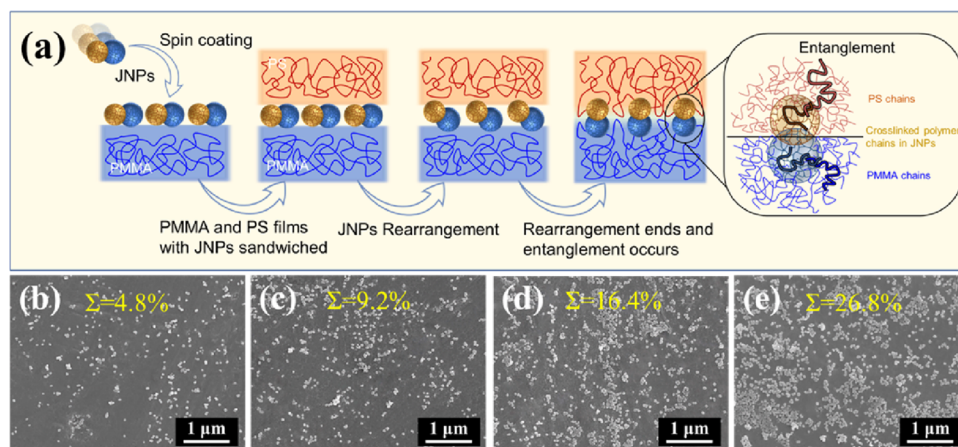


**Figure 11.** (a) Schematic illustration of the annealing rearrangement of JNPs at the PMMA/PS interface and subsequent penetration and entanglement with the bulk phases. (b–e) SEM images of JNP distributions at the interface of a PMMA/PS multilayer observed after a frequency sweep test at 220 °C with the PS films removed via selective etching. The feeding JNP concentration in the spin-coating solution was varied: (b) 0.1 wt %, (c) 0.3 wt %, (d) 1 wt %, and (e) 3 wt %.

increases with JNP concentration (Figure 9), regardless of the blend composition.

**3.3.2. Interfacial Relaxation Behavior in JNP-Sandwiched Multilayer Structures.** As mentioned above, the interfacial relaxation ( $\tau_\beta$ ) in blends is largely dependent on the droplet morphology, more exactly, the size of the separated domains, being closely coupled to the droplet shape relaxation ( $\tau_F$ ) process. Therefore, it is challenging to reveal and quantify the intrinsic contributions of compatibilizers to the interfacial viscoelasticity. To decouple the effect of morphology evolution and Marangoni stresses, here a multilayer system is constructed by alternatively assembling PMMA and PS films with JNPs sandwiched at the interface as a model system. This is envisaged to avoid the effect of droplet relaxation, morphology changes, and Marangoni stresses, thereby allowing to isolate the intrinsic interfacial viscoelasticity. It should be noted that in contrary to traditional interfacial rheology that imposes shear to generate a velocity gradient within the interface, in this case the shear flow field is applied such that the velocity gradient is perpendicular to the interface. However, due to the finite interfacial thickness, it is expected that interfacial relaxations will reveal themselves in this type of characterization as well.

To get dumbbell JNPs sandwiched at the interface between PMMA and PS films, a JNP dispersion was spin-coated onto one side of either a PMMA or a PS film and then the coated films were alternatively assembled to make sure every interface between neighboring PMMA/PS layers is laden with an identical amount of JNPs. The assembled multilayers with a total thickness of 1200  $\mu\text{m}$  but various numbers of layers (i.e., 2, 4, 6, 8, 10, and 12 layers) and various spin-coating concentrations (i.e., 0.1, 0.3, 1, and 3 wt %) were placed between parallel plates and annealed at 220 °C for 20 min to allow the JNPs to position correctly at the interface before being subjected to SAOS measurements. Figure 11a shows a schematic illustration of the JNP rearrangement at the PMMA/PS interface during the annealing process of sandwiched structures, whereby particle penetration into the bulk phases and chain entanglements between particles and the bulk become possible.

To quantify the actual amount of JNPs at the interface, after SAOS measurements, the multilayered specimens were

subjected to solvent etching to remove the PS layers and then the surface morphology of the remaining PMMA films was observed under SEM. As shown in Figure 11b–e, varying the spin-coating concentration from 0.1 to 3 wt %, the coverage of JNPs at the layer interface ( $\Sigma$ ) was correspondingly increased and determined by Image J (Fiji) software to be  $(4.8 \pm 0.3)\%$ ,  $(9.2 \pm 0.3)\%$ ,  $(16.4 \pm 0.5)\%$ , and  $(26.8 \pm 0.8)\%$ . It is worth noting that different from the dumbbell shape morphology of connected PMMA-PS spheres observed in Figure 4, the nanoparticles observed here are mostly single spheres, that is, the crosslinked PS spheres that remained undissolved and exposed to the air due to the etching of the PS layers, whereas the other half sides consisting of the PMMA spheres were embedded in the PMMA layers and unobservable. This confirms that the dumbbell JNPs played a “button” role in stitching the PMMA and PS layers via the dumbbell spheres. Moreover, at low  $\Sigma$ , the JNPs were hardly interconnected and remained separated while with increasing  $\Sigma$ , the JNPs became crowded at the interface with partial clusters/aggregates being formed.

Figure 12 shows the frequency dependence of  $G'$  and the  $H(\tau)*\tau$  curves of multilayer systems with various numbers of layer without and with JNPs (i.e.,  $\Sigma = 16.4\%$ ) at the interfaces. For a multilayer structure of incompatible polymers, it has been empirically demonstrated that the total rheological property can be described by a reciprocal addition rule of the component contributions,<sup>72</sup> that is,

$$\frac{1}{G'_{\text{Comp}}} = \frac{\phi_{\text{PMMA}}}{G'_{\text{PMMA}}} + \frac{\phi_{\text{PS}}}{G'_{\text{PS}}} \quad (11)$$

where  $G'_{\text{comp}}$ ,  $G'_{\text{PMMA}}$ , and  $G'_{\text{PS}}$  are the storage moduli of the layered composite, PMMA, and PS, respectively;  $\phi$  is the volume fraction. For comparison, data of the neat polymers and the predictions of the component contributions via eq 11 are also shown in Figure 12 as benchmarks. In great contrast to the distinct  $G'$  shoulder at low frequencies indicative of shape relaxation of droplets in blend systems (Figure 9), the  $G'$  curves of multilayer structures in the absence of JNPs almost follow the reciprocal addition rule (Figure 12a), exhibiting no secondary plateau for shape relaxation in the terminal region. Likewise, no peak indicative of shape relaxation was observed in the relaxation spectra (Figure 12b). This undoubtedly

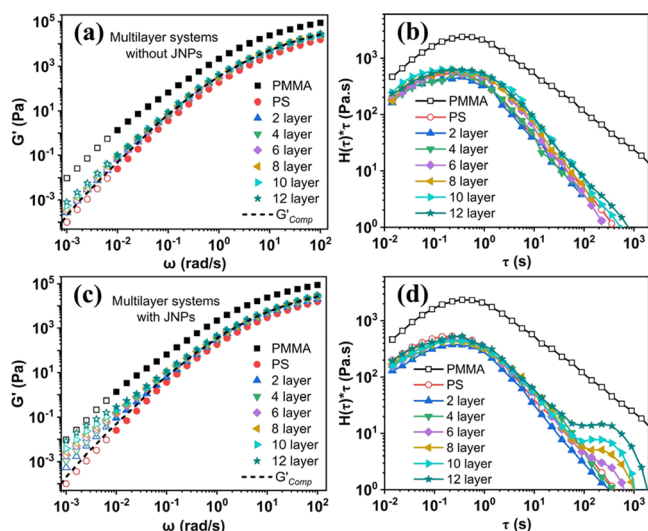


**Figure 12.** Frequency dependence of  $G'$  (a,c) and weighted relaxation time spectra (b,d) of multilayer systems with various layer numbers in the absence (a,b) and in the presence of JNPs ( $\Sigma = 16.4\%$ ) (c,d) at 220 °C. The dashed line is the total contribution of the neat components based on eq 11.

excludes the effect of droplet shape and morphology evolution on the LVE data in multilayer systems.

Intriguingly, in the multilayer systems with JNPs present at the interfaces, a clear shoulder at low frequencies (c.a.  $<10^{-2}$  rad/s) is observed and the shoulder becomes more pronounced with increasing number of layers (Figure 12c). Likewise, an additional relaxation process peaking around 250 s is observed in the relaxation time spectra with the time being nearly independent of the number of layers, while the peak height gradually increases when increasing the number of layers (Figure 12d). Undoubtedly, the new relaxation solely originates from contributions of the JNPs at the interfaces as an intrinsic interfacial relaxation. The corresponding timescale is indicated here as  $\tau'_{\beta}$  in analogy with  $\tau_{\beta}$  for the droplet-matrix blends. Note that by increasing the number of layers, the amount of JNPs in the whole system is increased, while the interfacial coverage is unchanged. This explains the independence of  $\tau'_{\beta}$  and the increase of the peak amplitude with the number of layers.

To identify the major relaxation processes, the generalized Maxwell model with multiple relaxation modes (eqs 12 and 13) was used to fit the LVE data of the multilayer systems with the number of modes determined by the RepTate software.<sup>73</sup>

$$G'(\omega) = \sum_1^{n_{\text{modes}}} G_i \frac{(\omega\tau_i)^2}{1 + (\omega\tau_i)^2} \quad (12)$$

$$G''(\omega) = \sum_1^{n_{\text{modes}}} G_i \frac{\omega\tau_i}{1 + (\omega\tau_i)^2} \quad (13)$$

where  $n_{\text{modes}}$  is the number of Maxwell modes uniformly distributed on a logarithmic scale between the minimum and maximum frequencies,  $G_i$  is the modulus, and  $\tau_i$  is the characteristic relaxation time ( $\sqrt{2}/\omega$ ) of mode  $i$ .

Figure 13a shows the frequency dependence of  $G'$  and  $G''$  for a 12-layer sample without JNPs ( $\Sigma = 0$ ) and a 12-layer sample with JNPs ( $\Sigma = 16.4\%$ ) at 220 °C as well as the fittings of the Maxwell model. After least-squares regression, 4 mode

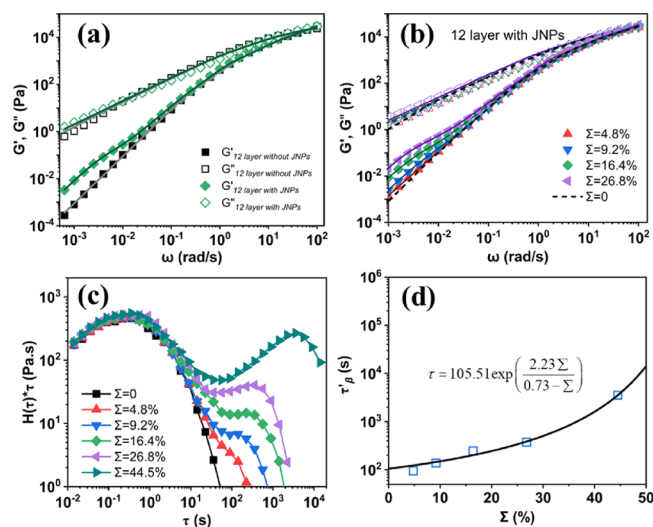


**Figure 13.** (a) Comparison of  $G'$  and  $G''$  with Maxwell model predictions at 220 °C for 12 layer structures sandwiched without and with dumbbell JNPs ( $\Sigma = 16.4\%$ ); (b)  $G'$  and  $G''$  of 12 layer samples with varied  $\Sigma$  of JNPs at 220 °C compared to Maxwell model predictions. Symbols are experimental data. The solid lines represent predictions of the Maxwell model, with 4 and 6 modes used for the 12-layer samples sandwiched without and with JNPs respectively. (c) Corresponding weighted relaxation time spectra. (d) Dependence of the weighted relaxation times on the JNPs  $\Sigma$  for 12-layer samples with JNPs at 220 °C, where the solid line is the fitting of VFT equation.

and 6 mode Maxwell models were found to the minimum required number of modes to give a sufficiently good fit in describing the relaxation behaviors of the 12-layer samples without and with JNPs, respectively, and the corresponding relaxation times obtained as fitting parameters are listed in Table 5. Relaxations of layered structures without JNPs are

**Table 5. Characteristic Relaxation Times Obtained by Fitting the Maxwell Model to the Neat Multilayers (Four Modes) and Multilayer Systems (Six Modes) with Different  $\Sigma$  of JNPs at 220 °C**

$\Sigma$ (%)	$\tau_1$ (s)	$\tau_2$ (s)	$\tau_3$ (s)	$\tau_4$ (s)	$\tau_5$ (s)	$\tau_6$ (s)
0	0.012	0.065	0.360	2.0		
4.8	0.029	0.155	0.814	4.3	22.4	117.6
9.2	0.014	0.095	0.635	4.2	28.2	186.4
16.4	0.011	0.083	0.632	4.8	36.4	275.7
26.8	0.010	0.081	0.668	5.6	46.8	389.5
44.5	0.005	0.078	1.171	17.5	260.9	3895.1

governed by the component polymers that exhibit a reptation relaxation of chain entanglements in a frequency region higher than that of the interfacial viscoelasticity due to the JNPs. Here, the four relaxation modes can be accounted for by the combination of PMMA and PS chains, each of which has a certain polydispersity in molecular weight. The component polymer relaxations in the 12-layer sample loaded with JNPs can also be interpreted with four relaxation modes in the high frequency region, while the enhanced elasticity at low frequencies can be described by two additional relaxation modes. The latter two modes ( $\tau_5$  and  $\tau_6$ ) are related to the JNPs at the interface and may be ascribed to, as mentioned above, entanglements between the free polymer chains in the bulk phase and polymer chains crosslinked in the polymeric

JNPs, as well as the escape of JNPs from their confined diffusion in a cage of a particle cluster (or a jammed state).

To further understand the two interfacial relaxations, the  $\Sigma$  of the JNPs at the interface was varied from 4.8 to 26.8%, and its effect on the LVE data of the multilayer systems was evaluated based on fittings of the 6 mode Maxwell model. Note that the morphology and LVE data for the sample of  $\Sigma = (44.5 \pm 1.2)\%$  are placed in Figure S10. As shown in Figure 13b, the elasticity enhancement at low frequencies increases with increasing  $\Sigma$  and the two fitted relaxation times ( $\tau_5$  and  $\tau_6$ ) are also strongly dependent on the  $\Sigma$ , with both increasing with  $\Sigma$  (Table 5). Likewise, the interfacial relaxation process ( $\tau'_\beta$ ) observed in the  $H(\tau)*\tau$  spectra (Figure 13c) is shifted to a higher time and becomes broader with increasing  $\Sigma$ . Here, the single process peaking at a timescale close to the fitted  $\tau_6$  might combine both  $\tau_5$  and  $\tau_6$ , with the latter being dominant. It is worth noting that this observation is opposite to the reduction of  $\tau_\beta$  with JNP concentration ( $w_{\text{JNPs}}$ ) observed in blend systems (see Figure 10). Undoubtedly, the increase of  $\tau'_\beta$  with  $\Sigma$  here can be ascribed to the increasing JNP jamming state at the interface as the escape time of JNPs from the cage of surrounding JNPs increases when JNPs become more crowded.<sup>74</sup> This opposite trend as compared to that in polymer blends confirms the different mechanism at play, namely, a dominance of Marangoni stresses in  $\tau_\beta$  for droplet-phase blends as compared to intrinsic viscoelasticity in the case of multilayers. Hence, this multilayer method overcomes the complexity of studying the intrinsic interfacial relaxation of particles,  $\tau'_\beta$ , in blend systems, where it is largely coupled to the effect of droplet size and morphology evolution, and so forth.

The observed dependence of  $\tau'_\beta$  on  $\Sigma$  is consistent with the cage effect widely reported in colloidal glasses in the bulk<sup>75</sup> and at liquid–liquid/(air) interfaces,<sup>29</sup> as well as the cage effect of nanoparticles observed in polymer nanocomposite systems.<sup>76</sup> To test this in a quantitative manner, the phenomenological VFT model that is commonly used to describe the divergent growth of the relaxation time with nanoparticles volume fraction in colloids<sup>77,78</sup> is also applied for our system. The VFT model has an expression as follows

$$\tau = \tau_0 \exp\left(\frac{A \Sigma}{\Sigma_{\text{RCP}} - \Sigma}\right) \quad (14)$$

where  $\tau_0$  is the relaxation time at low  $\Sigma$ ,  $\bar{A}$  is the strength of the  $\Sigma$  dependence of  $\tau$ , and  $\Sigma_{\text{RCP}}$  is the nominal interfacial coverage at RCP, all three of which were considered as fitting parameters. As shown in Figure 12d, the dependence of  $\tau$  on  $\Sigma$  can be well described by the VFT equation, verifying that the JNPs at the PMMA/PS molten interface follow the typical colloidal glass behavior with a cage effect, whereby the confined diffusion of particles in the cage is strongly dependent on the  $\Sigma$  with a divergence. The divergence was found to occur at  $\Sigma_{\text{RCP}} \sim 0.73$ , a value lower than that of conventional 2D packing (0.8–0.9),<sup>79</sup> which might be a result of possible effect from the interaction of JNPs with the bulk phase.

Likewise, the plateau moduli ( $G'_5$  and  $G'_6$ ) corresponding to  $\tau_5$  and  $\tau_6$  obtained from the Maxwell model can be plotted versus  $\Sigma$  for the 12-layered samples. As shown in Figure 14, both  $G'_5$  and  $G'_6$  increase with  $\Sigma$ , with the former having a more significant dependence. As mentioned above, the possible contributions to such interface-governed moduli are the entanglements between polymer chains crosslinked in the

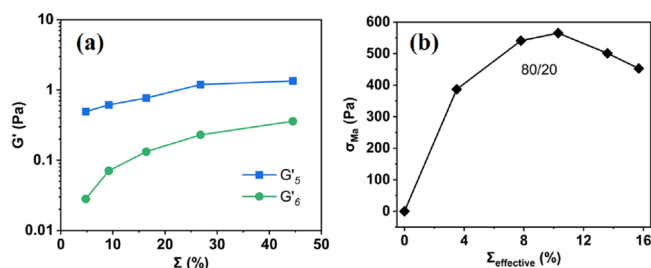


**Figure 14.** (a) Dependence of  $G'_5$  and  $G'_6$  on  $\Sigma$  for 12-layered samples with JNPs at 220 °C; (b) variation of Marangoni stress ( $\sigma_{\text{Ma}}$ ) with effective interfacial coverage ( $\Sigma_{\text{effective}}$ ) of JNPs for 80/20 blends at 200 °C.

JNPs and those from the bulk phase and the interfacial films consisting of jammed particles with a cage effect. Hence, it is evident that as the  $\Sigma$  increases, both the number of entanglements between JNPs and bulk chains and the interfacial jamming of particles is enhanced, and so is the interfacial viscoelasticity ( $G'_5$  and  $G'_6$ ). To compare with the interfacial shear modulus  $\beta_s$  obtained from droplet-matrix blends via the Palierne model, which involves combined contributions of Marangoni stresses and intrinsic interfacial rheology, here the dominant modulus  $G'_5$  was simply multiplied with the approximate interface thickness  $d$  (200 nm, approximated as the vertical length of the JNPs localizing at the interface) to describe the interfacial viscoelasticity in units of mN/m. For the 80/20/2.5 blend,  $\beta_s$  was determined to be 0.568 mN/m (Table 4) and the  $\Sigma$  was estimated to be 9.7%; here, for the multilayered system with a similar  $\Sigma$  of 9.2%,  $G'_5$  is  $\sim 0.6$  Pa and  $G'_5 \cdot d$  is estimated to be  $\sim 0.00012$  mN/m. This indicates that the intrinsic viscoelasticity of the particle-laden interface is several orders of magnitude lower than the Marangoni stress-dominated interfacial viscoelasticity, hence being easily overlooked in the analysis of blend systems. It should also be noted that the measurement protocol applied here provides the stiffness related to a shear rate gradient perpendicular to the interface rather than a shear rate gradient in the interface, which can contribute to the differences between the interfacial moduli obtained for the multilayer systems versus the blends. Likewise, the Marangoni stress ( $\sigma_{\text{Ma}}$ ) was estimated based on data for the 80/20 blends via  $\frac{\Sigma}{R_c} \left| \frac{d\Gamma}{d\Sigma} \right|$ <sup>20</sup> where  $\frac{d\Gamma}{d\Sigma}$  is the interfacial tension gradient with surface coverage, the absolute value of which can be determined from the curve of  $\Gamma$  versus  $\Sigma_{\text{effective}}$  (Figure S7). The results are given in Figure 14b, from which it is confirmed that the Marangoni stress is much larger than the intrinsic interfacial viscoelasticity of the JNPs (Figure 14a,  $G'_5$  and  $G'_6$ ) by several orders of magnitude, making the latter easily being overlooked. Meanwhile, in units of mN/m for the interface,  $\sigma_{\text{Ma}} \cdot d$  equates  $\sim 0.1$  mN/m, which is of the same order as  $\beta_s$  (i.e., 0.568 mN/m) determined from the Palierne model, confirming the dominance of the Marangoni stress in the interfacial viscoelasticity of blend systems.

#### 4. CONCLUSIONS

In this work, a fully polymeric dumbbell-shaped PMMA-PS JNPs with crosslinked PMMA and PS spheres of equal size ( $\sim 80$  nm) was prepared via seed emulsion polymerization and investigated as a compatibilizer for PMMA/PS blends. The chemical asymmetry and unique particle structure endows the JNPs with a good affinity to both PMMA and PS. This creates

a high chance that the particles localize at the PMMA/PS interface as demonstrated from their preferential coverage of the droplet interface in the blends. Both the droplet-matrix and co-continuous type morphologies were observed to be refined with increasing JNPs amount and a saturated state can be achieved with a JNPs concentration as low as 2.5 wt %. Hereby, a better compatibilization efficiency than that of block copolymers was observed, thereby confirming the interfacial activity of the JNPs. The linear viscoelasticity of the droplet-matrix blends was well fitted with the Palierne emulsion model, whereby the interfacial tension was determined to decrease from 1.23 mN/m at 0 wt % JNPs to 0.53 mN/m at 2.5 wt % JNPs, while the interfacial modulus  $\beta_s$  increases from 0.288 mN/m (with 0.5 wt % JNPs) to 0.568 mN/m (with 2.5 wt % JNPs). The  $G' - \omega$  curve of uncompatibilized PMMA/PS blends was characterized with a droplet shape relaxation ( $\tau_F$ ) shoulder in the low  $\omega$  region, and when JNPs were added, an additional interfacial relaxation ( $\tau_\beta$ ) shoulder was observed at lower  $\omega$  than that corresponding to  $\tau_F$ . The resulting relaxation peaks were clearly observed in the weighted relaxation spectrum ( $H(\tau) * \tau$ ). Here, the interfacial viscoelasticity of the JNPs can originate from three sources: elasticity of interfacial films formed by the JNPs, Marangoni stresses as a result of particle redistribution on the droplet surface, and entanglements between the crosslinked polymer chains in the JNPs and those from the bulk phase. The  $\tau_\beta$  was observed to monotonically decrease, in analogy to  $\tau_F$ , with increased JNP concentration and decreased volume fraction of dispersed phase, being a result of the reduced droplet size that accelerates relaxations of the droplet shape as well as of the gradients in particle distribution at the interface (Marangoni stresses). This indicates that the interfacial relaxation of JNPs obtained in blends is mainly governed by the morphological evolution and Marangoni stress effects, thereby masking the intrinsic contribution of the JNP viscoelastic films (governed by particle jamming and polymer entanglements, etc.) to the interfacial viscoelasticity.

Subsequently, a PMMA/PS multilayer structure with PMMA-PS dumbbell JNPs sandwiched at the planar interfaces was developed to decouple the effects of Marangoni stresses and morphological changes from the determination of the intrinsic interfacial viscoelasticity. In the multilayer structures without JNPs, no shape relaxation ( $\tau_F$ ) was observed, while in the presence of JNPs, an additional relaxation behavior was observed that can be ascribed to the intrinsic interfacial relaxation ( $\tau'_\beta$ ). In great contrast to the  $\tau_\beta$  in blends that decreased with increasing JNPs content, the  $\tau'_\beta$  in multilayer structures increased with JNP coverage ( $\Sigma$ ) at the interface, following the VFT model prediction for divergent behavior originating from the “cage” effect in classical colloidal glasses. In addition, the linear viscoelasticity of multilayer structures can be described with a multimode Maxwell model able to deconvolute the interfacial relaxation into two contributions: confined diffusion of JNPs within their cages and entanglements between crosslinked polymer chains in the JNPs and those from the bulk. This is the first time that the intrinsic interfacial contribution of particles at the interface of molten polymers is being revealed.

## ■ ASSOCIATED CONTENT

### SI Supporting Information

The Supporting Information is available free of charge at <https://pubs.acs.org/doi/10.1021/acs.macromol.2c01973>.

Linear viscoelasticity and thermal stability (i.e.,  $G'$  versus time) of neat polymers, synthesis route and FTIR data of PMMA-PS dumbbell-shaped JNPs and its loading method onto layer films, Cole–Cole plots and  $\Gamma - \Sigma_{\text{effective}}$  curve (fitted with eq 5) of PMMA/PS(80/20) blends with various JNPs amounts, additional data of linear viscoelasticity and relaxation spectra of PMMA/PS blends (90/10, 80/20, and 50/50) with various JNP amounts, and interfacial morphology and linear viscoelasticity of PMMA/PS multilayer sandwiched with JNPs at  $\Sigma = 44.5\%$  (PDF)

## ■ AUTHOR INFORMATION

### Corresponding Author

**Huagui Zhang** – College of Chemistry and Materials Science, Fujian Key Laboratory of Polymer Materials, Fujian Provincial Key Laboratory of Advanced Materials Oriented Chemical Engineering, Fujian Normal University, Fuzhou 350007, China; [orcid.org/0000-0003-2438-788X](https://orcid.org/0000-0003-2438-788X); Email: [huagui.zhang@fjnu.edu.cn](mailto:huagui.zhang@fjnu.edu.cn)

### Authors

**Huawei Qiao** – College of Chemistry and Materials Science, Fujian Key Laboratory of Polymer Materials, Fujian Provincial Key Laboratory of Advanced Materials Oriented Chemical Engineering, Fujian Normal University, Fuzhou 350007, China; [orcid.org/0000-0001-6953-7592](https://orcid.org/0000-0001-6953-7592)

**Botuo Zheng** – College of Chemistry and Materials Science, Fujian Key Laboratory of Polymer Materials, Fujian Provincial Key Laboratory of Advanced Materials Oriented Chemical Engineering, Fujian Normal University, Fuzhou 350007, China

**Gang Zhong** – College of Chemistry and Materials Science, Fujian Key Laboratory of Polymer Materials, Fujian Provincial Key Laboratory of Advanced Materials Oriented Chemical Engineering, Fujian Normal University, Fuzhou 350007, China

**Zhicong Li** – College of Chemistry and Materials Science, Fujian Key Laboratory of Polymer Materials, Fujian Provincial Key Laboratory of Advanced Materials Oriented Chemical Engineering, Fujian Normal University, Fuzhou 350007, China

**Ruth Cardinaels** – Soft Matter Rheology and Technology, Department of Chemical Engineering, KU Leuven, B-3001 Leuven, Belgium; [orcid.org/0000-0002-4191-6504](https://orcid.org/0000-0002-4191-6504)

**Paula Moldenaers** – Soft Matter Rheology and Technology, Department of Chemical Engineering, KU Leuven, B-3001 Leuven, Belgium; [orcid.org/0000-0003-4197-2626](https://orcid.org/0000-0003-4197-2626)

**Khalid Lamnawar** – Université de Lyon, CNRS, UMR 5223, Ingénierie des Matériaux Polymères, INSA Lyon, Université Claude Bernard Lyon 1, Université Jean Monnet, Villeurbanne F-69621, France; [orcid.org/0000-0003-4907-0977](https://orcid.org/0000-0003-4907-0977)

**Abderrahim Maazouz** – Université de Lyon, CNRS, UMR 5223, Ingénierie des Matériaux Polymères, INSA Lyon, Université Claude Bernard Lyon 1, Université Jean Monnet, Villeurbanne F-69621, France

**Canpei Liu** – College of Chemistry and Materials Science, Fujian Key Laboratory of Polymer Materials, Fujian Provincial Key Laboratory of Advanced Materials Oriented Chemical Engineering, Fujian Normal University, Fuzhou 350007, China

Complete contact information is available at:  
<https://pubs.acs.org/10.1021/acs.macromol.2c01973>

## Notes

The authors declare no competing financial interest.

## ACKNOWLEDGMENTS

This work was financially supported by the National Natural Science Foundation of China (21903015; 22172028; and 22111530080), the Natural Science Foundation of Fujian Province of China (2020J01145 and 2022J05041), the Fujian Provincial Health Education Joint Research Project (WKJ2016-2-11), the Award Program of Fujian Minjiang Scholar Professorship (2018), and the Research Foundation – Flanders FWO (VS04421N).

## REFERENCES

- (1) Scott, C. E.; Macosko, C. W. Morphology development during the initial stages of polymer-polymer blending. *Polymer* **1995**, *36*, 461–470.
- (2) Utracki, L. A.; Shi, Z. H. Development of polymer blend morphology during compounding in a twin-screw extruder. Part I: Droplet dispersion and coalescence—a review. *Polym. Eng. Sci.* **1992**, *32*, 1824–1833.
- (3) López-Barrón, C. R.; Macosko, C. W. Rheology of compatibilized immiscible blends with droplet-matrix and cocontinuous morphologies during coarsening. *J. Rheol.* **2014**, *58*, 1935–1953.
- (4) Huang, S.; Bai, L.; Trifkovic, M.; Cheng, X.; Macosko, C. W. Controlling the Morphology of Immiscible Cocontinuous Polymer Blends via Silica Nanoparticles Jammed at the Interface. *Macromolecules* **2016**, *49*, 3911–3918.
- (5) Bai, L.; He, S.; Fruehwirth, J. W.; Stein, A.; Macosko, C. W.; Cheng, X. Localizing graphene at the interface of cocontinuous polymer blends: Morphology, rheology, and conductivity of cocontinuous conductive polymer composites. *J. Rheol.* **2017**, *61*, 575–587.
- (6) Trifkovic, M.; Hedegaard, A. T.; Sheikhzadeh, M.; Huang, S.; Macosko, C. W. Stabilization of PE/PEO Cocontinuous Blends by Interfacial Nanoclays. *Macromolecules* **2015**, *48*, 4631–4644.
- (7) Pickering, S. U. Cxvi.—emulsions. *J. Chem. Soc., Trans.* **1907**, *91*, 2001–2021.
- (8) Walther, A.; Hoffmann, M.; Müller, A. H. E. Emulsion Polymerization Using Janus Particles as Stabilizers. *Angew. Chem., Int. Ed.* **2008**, *47*, 711–714.
- (9) Caro, A. S.; Parpaite, T.; Otazaghine, B.; Taguet, A.; Lopez-Cuesta, J. M. Viscoelastic properties of polystyrene/polylamide-6 blend compatibilized with silica/polystyrene Janus hybrid nanoparticles. *J. Rheol.* **2017**, *61*, 305–310.
- (10) Cardinaels, R., Chapter 8 - Compatibilization of polymer blends by Janus particles. In *Compatibilization of Polymer Blends*; Ajitha, A. R.; Thomas, S., Eds.; Elsevier, 2020; pp 249–275.
- (11) Anastasiadis, S. H.; Gancarz, I.; Koberstein, J. T. Compatibilizing effect of block copolymers added to the polymer/polymer interface. *Macromolecules* **1989**, *22*, 1449–1453.
- (12) Lyu, S.; Jones, T. D.; Bates, F. S.; Macosko, C. W. Role of Block Copolymers on Suppression of Droplet Coalescence. *Macromolecules* **2002**, *35*, 7845–7855.
- (13) Sundararaj, U.; Macosko, C. W. Drop Breakup and Coalescence in Polymer Blends: The Effects of Concentration and Compatibilization. *Macromolecules* **1995**, *28*, 2647–2657.
- (14) Genoyer, J.; Yee, M.; Soulestin, J.; Demarquette, N. Compatibilization mechanism induced by organoclay in PMMA/PS blends. *J. Rheol.* **2017**, *61*, 613–626.
- (15) Macosko, C. W.; Guégan, P.; Khandpur, A. K.; Nakayama, A.; Marechal, P.; Inoue, T. Compatibilizers for Melt Blending: Premade Block Copolymers. *Macromolecules* **1996**, *29*, 5590–5598.
- (16) Ha, J. W.; Yoon, Y.; Leal, L. G. The effect of compatibilizer on the coalescence of two drops in flow. *Phys. Fluids* **2003**, *15*, 849–867.
- (17) Zhu, X.; Kong, M.; Lv, Y.; Huang, Y.; Li, G. Selective distribution of nanoparticles in immiscible blends: Effects on the morphology evolution and rheology in quiescent annealing, shear and extensional flow. *J. Rheol.* **2020**, *64*, 1357–1371.
- (18) Beuguel, Q.; Guinault, A.; Chinesta, F.; Sollogoub, C.; Miquelard-Garnier, G. Modeling of the rheological properties of multilayer films in the presence of compatibilized interphase. *J. Rheol.* **2020**, *64*, 981–989.
- (19) Van Hemelrijck, E.; Van Puyvelde, P.; Velankar, S.; Macosko, C. W.; Moldenaers, P. Interfacial elasticity and coalescence suppression in compatibilized polymer blends. *J. Rheol.* **2003**, *48*, 143–158.
- (20) Van Hemelrijck, E.; Van Puyvelde, P.; Macosko, C. W.; Moldenaers, P. The effect of block copolymer architecture on the coalescence and interfacial elasticity in compatibilized polymer blends. *J. Rheol.* **2005**, *49*, 783–798.
- (21) Graebing, D.; Muller, R.; Palierne, J. F. Linear viscoelastic behavior of some incompatible polymer blends in the melt. Interpretation of data with a model of emulsion of viscoelastic liquids. *Macromolecules* **1993**, *26*, 320–329.
- (22) Castro, M.; Carrot, C.; Prochazka, F. Experimental and theoretical description of low frequency viscoelastic behaviour in immiscible polymer blends. *Polymer* **2004**, *45*, 4095–4104.
- (23) Yu, W.; Zhou, W.; Zhou, C. Linear viscoelasticity of polymer blends with co-continuous morphology. *Polymer* **2010**, *51*, 2091–2098.
- (24) Silva, J.; Machado, A. V.; Moldenaers, P.; Maia, J. The effect of interfacial properties on the deformation and relaxation behavior of PMMA/PS blends. *J. Rheol.* **2010**, *54*, 797–813.
- (25) Huitric, J.; Ville, J.; Médéric, P.; Moan, M.; Aubry, T. Rheological, morphological and structural properties of PE/PA/nanoclay ternary blends: Effect of clay weight fraction. *J. Rheol.* **2009**, *53*, 1101–1119.
- (26) Riemann, R. E.; Cantow, H. J.; Friedrich, C. Interpretation of a New Interface-Governed Relaxation Process in Compatibilized Polymer Blends. *Macromolecules* **1997**, *30*, 5476–5484.
- (27) Palierne, J. F. Linear rheology of viscoelastic emulsions with interfacial tension. *Rheol. Acta* **1990**, *29*, 204–214.
- (28) Jacobs, U.; Fahrlander, M.; Winterhalter, J.; Friedrich, C. Analysis of Palierne's emulsion model in the case of viscoelastic interfacial properties. *J. Rheol.* **1999**, *43*, 1495–1509.
- (29) Zhang, H.; Yu, K.; Cayre, O. J.; Harbottle, D. Interfacial Particle Dynamics: One and Two Step Yielding in Colloidal Glass. *Langmuir* **2016**, *32*, 13472–13481.
- (30) Sillescu, H. Heterogeneity at the glass transition: a review. *J. Non-Cryst. Solids* **1999**, *243*, 81–108.
- (31) Krieger, I. M.; Dougherty, T. J. A Mechanism for Non-Newtonian Flow in Suspensions of Rigid Spheres. *Trans. Soc. Rheol.* **1959**, *3*, 137–152.
- (32) Hunter, G. L.; Weeks, E. R. The physics of the colloidal glass transition. *Rep. Prog. Phys.* **2012**, *75*, No. 066501.
- (33) Orsi, D.; Cristofolini, L.; Baldi, G.; Madsen, A. Heterogeneous and Anisotropic Dynamics of a 2D Gel. *Phys. Rev. Lett.* **2012**, *108*, No. 105701.
- (34) Zhang, H.; Lamnawar, K.; Maazouz, A.; Maia, J. M. A nonlinear shear and elongation rheological study of interfacial failure in compatible bilayer systems. *J. Rheol.* **2015**, *60*, 1–23.
- (35) Zhao, W.; Zhang, M.; Zhang, H.; Shen, J.; Lu, B.; Dong, B.; Liu, C.; Maazouz, A.; Lamnawar, K. Roles of Interlayer Diffusion and Confinements in Manipulating Microstructural Evolutions in Multilayer Assembled Polyvinylidene Fluoride/Poly(methyl methacrylate) Films for Tunable Dielectric and Piezoelectric Performances. *ACS Appl. Polym. Mater.* **2021**, *3*, 3843–3854.
- (36) Zhang, H.; Lamnawar, K.; Maazouz, A. Rheological Modeling of the Mutual Diffusion and the Interphase Development for an Asymmetrical Bilayer Based on PMMA and PVDF Model Compatible Polymers. *Macromolecules* **2013**, *46*, 276–299.

- (37) Jordan, A. M.; Lee, B.; Kim, K.; Ludtke, E.; Lhost, O.; Jaffer, S. A.; Bates, F. S.; Macosko, C. W. Rheology of polymer multilayers: Slip in shear, hardening in extension. *J. Rheol.* **2019**, *63*, 751–761.
- (38) Zhang, H.; Lamnawar, K.; Maazouz, A. Fundamental understanding and modeling of diffuse interphase properties and its role in interfacial flow stability of multilayer polymers. *Polym. Eng. Sci.* **2015**, *55*, 771–791.
- (39) Lu, B.; Lamnawar, K.; Maazouz, A. Rheological and dynamic insights into an in situ reactive interphase with graft copolymers in multilayered polymer systems. *Soft Matter* **2017**, *13*, 2523–2535.
- (40) Zhao, R.; Macosko, C. W. Slip at polymer–polymer interfaces: Rheological measurements on coextruded multilayers. *J. Rheol.* **2002**, *46*, 145–167.
- (41) Liu, C. Y.; He, J. S.; van Ruymbeke, E.; Keunings, R.; Bailly, C. Evaluation of different methods for the determination of the plateau modulus and the entanglement molecular weight. *Polymer* **2006**, *47*, 4461–4479.
- (42) Schindelin, J.; Arganda-Carreras, I.; Frise, E.; Kaynig, V.; Longair, M.; Pietzsch, T.; Preibisch, S.; Rueden, C.; Saalfeld, S.; Schmid, B.; Tinevez, J.-Y.; White, D. J.; Hartenstein, V.; Eliceiri, K.; Tomancak, P.; Cardona, A. Fiji: an open-source platform for biological-image analysis. *Nat. Methods* **2012**, *9*, 676–682.
- (43) Bahrami, R.; Löbbling, T. I.; Gröschel, A. H.; Schmalz, H.; Müller, A. H. E.; Altstädt, V. The Impact of Janus Nanoparticles on the Compatibilization of Immiscible Polymer Blends under Technologically Relevant Conditions. *ACS Nano* **2014**, *8*, 10048–10056.
- (44) Parpaité, T.; Otazaghine, B.; Caro, A. S.; Taguet, A.; Sonnier, R.; Lopez-Cuesta, J. M. Janus hybrid silica/polymer nanoparticles as effective compatibilizing agents for polystyrene/polyamide-6 melted blends. *Polymer* **2016**, *90*, 34–44.
- (45) Weiss, S.; Hirsemann, D.; Biersack, B.; Ziadeh, M.; Müller, A. H. E.; Brey, J. Hybrid Janus particles based on polymer-modified kaolinite. *Polymer* **2013**, *54*, 1388–1396.
- (46) Ashcraft, E.; Ji, H.; Mays, J.; Dadmun, M. A Novel Reactive Processing Technique: Using Telechelic Polymers To Reactively Compatibilize Polymer Blends. *ACS Appl. Mater. Interfaces* **2009**, *1*, 2163–2173.
- (47) You, W.; Yu, W. Onset Reduction and Stabilization of Cocontinuous Morphology in Immiscible Polymer Blends by Snowmanlike Janus Nanoparticles. *Langmuir* **2018**, *34*, 11092–11100.
- (48) Graham, R. L.; Lubachevsky, B. D.; Nurmela, K. J.; Östergård, P. R. J. Dense packings of congruent circles in a circle. *Discrete Math.* **1998**, *181*, 139–154.
- (49) Schwarzl, F. R. The numerical calculation of storage and loss compliance from creep data for linear viscoelastic materials. *Rheol. Acta* **1969**, *8*, 6–17.
- (50) Muenstedt, H.; Katsikis, N.; Kaschta, J. Rheological Properties of Poly(methyl methacrylate)/Nanoclay Composites As Investigated by Creep Recovery in Shear. *Macromolecules* **2008**, *41*, 9777–9783.
- (51) Shaayegan, V.; Wood-Adams, P.; Demarquette, N. R. Linear viscoelasticity of immiscible blends: The application of creep. *J. Rheol.* **2012**, *56*, 1039–1056.
- (52) Afsari, B.; Razavi Aghjeh, M. K.; Hasanpour, M. Evolution of morphology and morphology stability in PP/PA6/EPDM-g-MA reactive ternary blends using viscoelastic measurements. *Rheol. Acta* **2020**, *59*, 399–414.
- (53) Calvão, P. S.; Yee, M.; Demarquette, N. R. Effect of composition on the linear viscoelastic behavior and morphology of PMMA/PS and PMMA/PP blends. *Polymer* **2005**, *46*, 2610–2620.
- (54) Vinckier, I.; Moldenaers, P.; Mewis, J. Relationship between rheology and morphology of model blends in steady shear flow. *J. Rheol.* **1996**, *40*, 613–631.
- (55) Lacroix, C.; Aressy, M.; Carreau, P. J. Linear viscoelastic behavior of molten polymer blends: A comparative study of the Palierne and Lee and Park models. *Rheol. Acta* **1997**, *36*, 416–428.
- (56) Valera, T. S.; Morita, A. T.; Demarquette, N. R. Study of Morphologies of PMMA/PP/PS Ternary Blends. *Macromolecules* **2006**, *39*, 2663–2675.
- (57) Genoyer, J.; Soulestin, J.; Demarquette, N. R. Influence of the molar masses on compatibilization mechanism induced by two block copolymers in PMMA/PS blends. *J. Rheol.* **2018**, *62*, 681–693.
- (58) Elias, L.; Fenouillot, F.; Majeste, J. C.; Cassagnau, P. Morphology and rheology of immiscible polymer blends filled with silica nanoparticles. *Polymer* **2007**, *48*, 6029–6040.
- (59) Kerner, E. H. The Elastic and Thermo-elastic Properties of Composite Media. *Proc. Phys. Soc. Sect. B* **1956**, *69*, 808–813.
- (60) Gramespacher, H.; Meissner, J. Melt elongation and recovery of polymer blends, morphology, and influence of interfacial tension. *J. Rheol.* **1997**, *41*, 27–44.
- (61) Tang, T.; Huang, B. Interfacial behaviour of compatibilizers in polymer blends. *Polymer* **1994**, *35*, 281–285.
- (62) Yee, M.; Calvão, P. S.; Demarquette, N. R. Rheological behavior of poly(methyl methacrylate)/polystyrene (PMMA/PS) blends with the addition of PMMA-ran-PS. *Rheol. Acta* **2007**, *46*, 653–664.
- (63) Wu, S. Formation of dispersed phase in incompatible polymer blends: Interfacial and rheological effects. *Polym. Eng. Sci.* **1987**, *27*, 335–343.
- (64) Wang, H.; Fu, Z.; Zhao, X.; Li, Y.; Li, J. Reactive Nanoparticles Compatibilized Immiscible Polymer Blends: Synthesis of Reactive SiO<sub>2</sub> with Long Poly(methyl methacrylate) Chains and the in Situ Formation of Janus SiO<sub>2</sub> Nanoparticles Anchored Exclusively at the Interface. *ACS Appl. Mater. Interfaces* **2017**, *9*, 14358–14370.
- (65) Everaert, V.; Aerts, L.; Groeninckx, G. Phase morphology development in immiscible PP/(PS/PPE) blends influence of the melt-viscosity ratio and blend composition. *Polymer* **1999**, *40*, 6627–6644.
- (66) Jana, S. C.; Sau, M. Effects of viscosity ratio and composition on development of morphology in chaotic mixing of polymers. *Polymer* **2004**, *45*, 1665–1678.
- (67) Honerkamp, J.; Weese, J. A nonlinear regularization method for the calculation of relaxation spectra. *Rheol. Acta* **1993**, *32*, 65–73.
- (68) Li, R.; Yu, W.; Zhou, C. Rheological Characterization of Droplet-Matrix versus Co-Continuous Morphology. *J. Macromol. Sci., Part B: Phys.* **2006**, *45*, 889–898.
- (69) Weis, C.; Leukel, J.; Borkenstein, K.; Maier, D.; Gronski, W.; Friedrich, C.; Honerkamp, J. Morphological and rheological detection of the phase inversion of PMMA/PS polymer blends. *Polym. Bull.* **1998**, *40*, 235–241.
- (70) López-Barrón, C. R.; Macosko, C. W. A new model for the coarsening of cocontinuous morphologies. *Soft Matter* **2010**, *6*, 2637–2647.
- (71) López-Barrón, C. R.; Macosko, C. W. Rheological and morphological study of cocontinuous polymer blends during coarsening. *J. Rheol.* **2012**, *56*, 1315–1334.
- (72) Zhang, H.; Lamnawar, K.; Maazouz, A. Rheological modeling of the diffusion process and the interphase of symmetrical bilayers based on PVDF and PMMA with varying molecular weights. *Rheol. Acta* **2012**, *51*, 691–711.
- (73) Boudara, V. A. H.; Read, D. J.; Ramírez, J. RepTate rheology software: Toolkit for the analysis of theories and experiments. *J. Rheol.* **2020**, *64*, 709–722.
- (74) Sciortino, F.; Tartaglia, P. Glassy colloidal systems. *Adv. Phys.* **2005**, *54*, 471–524.
- (75) Mewis, J.; Wagner, N. J. *Colloidal suspension rheology*; Cambridge university press, 2011.
- (76) You, W.; Yu, W. Slow Linear Viscoelastic Relaxation of Polymer Nanocomposites: Contribution from Confined Diffusion of Nanoparticles. *Macromolecules* **2019**, *52*, 9094–9104.
- (77) Wang, J. G.; Li, Q.; Peng, X.; McKenna, G. B.; Zia, R. N. “Dense diffusion” in colloidal glasses: short-ranged long-time self-diffusion as a mechanistic model for relaxation dynamics. *Soft Matter* **2020**, *16*, 7370–7389.
- (78) Nigro, V.; Angelini, R.; Bertoldo, M.; Bruni, F.; Ricci, M. A.; Ruzicka, B. Dynamical behavior of microgels of interpenetrated polymer networks. *Soft Matter* **2017**, *13*, 5185–5193.

(79) Milz, L.; Schmiedeberg, M. Connecting the random organization transition and jamming within a unifying model system. *Phys. Rev. E* **2013**, *88*, No. 062308.

## Recommended by ACS

---

### Impact of Topological Parameters on Melt Rheological Properties and Foamability of PS POM-POMs

Marie-Christin Röpert, Manfred Wilhelm, *et al.*

FEBRUARY 23, 2023  
MACROMOLECULES

READ 

---

### Mismatch in Nematic Interactions Leads to Composition-Dependent Crystal Nucleation in Polymer Blends

Wenlin Zhang and Lingyi Zou

MARCH 07, 2023  
MACROMOLECULES

READ 

---

### Chain Flexibility Effects on the Self-Assembly of Diblock Copolymer in Thin Films

Mingyang Chen, Xingkun Man, *et al.*

FEBRUARY 07, 2023  
MACROMOLECULES

READ 

---

### Selective Swelling of Polystyrene (PS)/Poly(dimethylsiloxane) (PDMS) Block Copolymers in Alkanes

Shoutian Qiu, Yong Wang, *et al.*

DECEMBER 26, 2022  
MACROMOLECULES

READ 

---

Get More Suggestions >

---